PONTIFICIA UNIVERSIDAD CATOLICA DE CHILE
SCHOOL OF ENGINEERING

USING THE WEATHER RESEARCH AND FORECASTING (WRF) MODEL FOR PRECIPITATION FORECASTING IN AN ANDEAN REGION WITH COMPLEX TOPOGRAPHY

GONZALO JOSÉ YÁÑEZ MORRONI

Thesis submitted to the Office of Research and Graduate Studies
in partial fulfillment of the requirements for the degree of
Master in Engineering Sciences

Advisor:
JORGE GIRONÁS LEÓN

Santiago de Chile, Junio 2018

PONTIFICIA UNIVERSIDAD CATOLICA DE CHILE
SCHOOL OF ENGINEERING

USING THE WEATHER RESEARCH AND FORECASTING (WRF) MODEL FOR PRECIPITATION FORECASTING IN AN ANDEAN REGION WITH COMPLEX TOPOGRAPHY

GONZALO JOSÉ YÁÑEZ MORRONI

Members of the Committee:
JORGE GIRONÁS LEÓN
CRISTIÁN ESCAURIAZA MESA
RENÉ GARREAUD SALAZAR
LUCIANO CHIANG SÁNCHEZ

Thesis submitted to the Office of Research and Graduate Studies
in partial fulfillment of the requirements for the degree of
Master in Engineering Sciences

Santiago de Chile, Junio 2018

Si una puerta se cierra, doscientas
se abren

ACKNOWLEDGEMENTS

Agradezco en nuestro dialecto, pues en mis costumbres, es el idioma que he ocupado para pensar y sentir. Doy gracias a mi familia, por todos los años de ausencia y silencio que tuve, y por aceptar mis cambios. A mis padres, por dar tanto de su vida y tiempo al procurarnos todo el amor, paciencia y abrigo que pudieron. Incluso en sus días de descanso.

De los grandes maestros que he tenido, Jorge Gironás. Por confiar en mí y aconsejarme en todas las dudas que tuve, en especial las de vida, música y letras. A él mi gran admiración, por bosquejar y refinar la arquitectura interna que constituyen hoy esta tesis. Agradezco tambien al Maestro Jahnke, por guiarme en el difícil camino del canto y la ingeniería. Y a René Garreaud, quien ayudó, con la maestría de pocos, a delimitar finalmente esta investigación.

Doy gracias al apoyo entregado por ND-PUC Seed Fund y el equipo docente involucrado, como también al financiamiento de las becas "Arturo Cousiño Lyon" y Magíster Nacional CONICYT. Agradezco también a los proyectos de investigación FONDECYT 1161439, y CIGIDEN/FONDAP 15110017 y CEDEUS/FONDAP 15110020. Y finalmente a la SOCHID, que me permitió trabajar y conocer admirables voces de la Hidráulica.

A mis compañeros de carrera, aunque con tanta distancia en el tiempo: sepan ustedes que las exigencias semanales siempre fueron posibles por estar en comunión. A mis compañeros de Magíster, sobre todo a aquellos que con valentía abandonaron el progama. Y a los que aún quedan, Andrés, Hoch, Lucho Piñén: que el esfuerzo no se vaya en collera. Mis mejores recuerdos y gratitud a Metrología, tercer piso, gloria de antaño y aspiración capitalina del mítico "Nunca Se Supo" . También a mis amigos del CCG, que alegran mis dias hábiles con la sabiduría de David Hackenherr.

A Belén, por todos los lugares en que bailamos. A La Fore, por entregar amor eterno en cada libro. A Dalinka, por quererme antes de que yo me conociera. Y a cada señora de tango, en todos los abrazos de tantas milongas. Por tanto sentir compartido sin palabras.

A mis amigos de coro, por darle vida al canto en toda reunión: único trabajo en grupo equitativo y satisfactorio en esta vida. Todo se resume a la perfección de un momento.

A mis amigos de cueca, maestría y pichicateo con huichipirichi en el canto a la rueda: los amigos de Puente, El Rubio, Ciego Jorge, Cabro Yohan, Juanito, El Monrero, La Caro, Lucho Piñén, Mateo, entre tantos.

Pero entre tantos, sólo a Mateo puedo agradecer por enseñarme y aprenderme. No tengo palabras para tí, solo las canciones harán justicia a mis defectos y sentimientos.

TABLE OF CONTENTS

LIST OF FIGURES

LIST OF TABLES

ABSTRACT

The Weather Research and Forecasting (WRF) model has been successfully used in weather prediction, but its ability to simulate atmospheric conditions over areas with complex topography is not optimal. Consequently, WRF has some problems when forecasting rainfall events over Chilean mountainous terrain and foothills, which are precisely where some of the main cities are located and the more intense rainfall events, caused by the presence of cut-off lows, take place. This work analyzes an ensemble of physics schemes to enhance initial forecasts made by the Chilean Weather Agency (DMC), in the Quebrada de Ramón catchment, located in the front range of the andes in Central Chile. We first tested different vertical levels resolution, land use and land surface models, as well as initial and boundary condition data (GFS/FNL). The final ensemble configuration considered three microphysics schemes and lead times over three rainfall events between 2015 and 2017. Cutoff low complex meteorological characteristics difficult the simulation of rainfall properties, such as peak intensity, rainfall beginning and temporal distribution. Nevertheless, with a lead time of 3 days, WRF properly forecasts the rainiest N-hours and temperatures during the event, although more accuracy is obtained when the rainfall is caused by a meteorological frontal system. Finally, the WSM6 microphysics option was chosen as the one with best forecast performance, although the further analysis using other storms and locations in the area are needed to strengthen this result. Further testing in this region is required, compromising a geostatistical approach to countervail WRF forecasts shortcomings over Andean piedmont.

Keywords: WRF forecast, rainfall, complex topography, Andean watershed, flash floods

RESUMEN

El Modelo para la Predicción e Investigación del Clima (WRF, en inglés) se ha usado exitosamente en pronósticos meteorológicos, pero su habilidad para capturar las condiciones atmosf'éricas sobre terrenos complejos no es óptima. Por tanto, WRF presenta problemas en las simulaciones hechas sobre la topografía precordillerana y andina de Chile, precisamente el lugar donde se ubican las ciudades principales y ocurren los eventos más intensos de precipitación, causados por la presencia de bajas segregadas. Este trabajo analiza un ensamble de esquemas físicos para mejorar los pronósticos realizados por la Dirección Meteorológica de Chile, en la cuenca precordillerana de Quebrada de Ramón, en Santiago. Inicialmente se evalúa la resolución vertical, uso de suelo, parametrizaciones de esquemas de superficie terrestre (LSM, en inglés) y las forzantes meteorológicas iniciales y de condiciones de borde (GFS/FNL). La configuración final del ensamble fue hecha considerando tres esquemas de microfísica, y tres tiempos de anticipo al pronóstico (lead time, en inglés) sobre tres eventos de precipitación ocurridos entre 2015 y 2017. Las características meteorológicas propias de la configuración de una baja segregada dificultan la simulación de la lluvia y alguna de sus características, como la intensidad máxima, el exacto inicio de la lluvia y su distibución temporal. Sin embargo, cuando se considera un tiempo de anticipo de 3 días, WRF predice correctamente tanto las N horas consecutivas más lluviosas, como también las temperaturas durante el evento. Esta predicción mejora cuando la lluvia es causada por un sistema frontal, reduciéndose así las incertidumbres del pronóstico. Finalmente, la opción microfísica de WSM6 fue escogida como aquella que simula mejor los eventos de precipitación, aunque se hace necesario más investigación para calibrar WRF en esta región.

Palabras Claves: WRF, lluvia, topografía compleja, aluvión, cuencas precordilleranas

1. INTRODUCTION

Natural disasters with hydrological, meteorological or climatological origin are a severe and worldwide problem which causes loss of life and property damage (EM-DAT, 2016). Global warming appears to be positively correlated with future flood risk at global scale: an increasement of $4°$C will drastically increase flood risk in several countries representing $\sim 70\%$ of the world population (Alfieri et al., 2016). Unevenness in future rainfall projections over South America doesn't facilitate future flood risk projections, althought in the past two decades several flood events took place in Andean regions (Kundzewicz et al. (2014) and references therein). For example, Chile's Atacama Desert - the driest desert in the world - recorded 65 mm of rainfall in just 3 days in March 2015 (Bozkurt et al., 2016; Wilcox et al., 2016). This rainfall unleashed a torrential flood due to the combined effect of high temperatures, a steep topography and erosion favored by the soil granulometry and its infiltration capacity (DGA, 2016). The event caused several human loses, the interruption of water and electricity supplies for weeks and an estimated economic cost of $\sim$ US\$ 1.5 billions (Otarola et al., 2016).

Numerical weather prediction (NWP) models are broadly and successfully used for weather prediction and research. However, the simulation of rain events over complex orography (i.e. mountaneous regions) is still a challenge, as NWP models may not resolve the underlying topography within a high resolution (Arnold et al., 2012; Goger et al., 2016). Futhermore, complex topography affects the meteorology by modifying the surface heat flux, albedo, wind speed and direction (Bongioannini Cerlini et al., 2005; Houze, 2012; Jiménez & Dudhia, 2012; Lorente-Plazas et al., 2016). A description of this complex topography helps to understand the behavior of the planet boundary layer (PBL) and microphysics (MP) schemes, allowing to study the slope wind-flow and valley wind-flow. However, none of the PBL parameterizations accurately predict the abrupt wind speeds and temperature profiles near the surface (Madala et al., 2014; Dimitrova et al., 2016; Siuta et al., 2017). Increasing the vertical resolution of the computation grid near the ground-surface has been done to improve the modeling results in places with complex topography (Pontoppidan et al., 2017). The finer grid provides more details in complex orographic zones, and a better performance depending on the regional climatology (Mass et al., 2002). Nevertheless, a finer domain grid resolution has a limted impact on the traditional verification scores, and it doesn't always improve the rainfall forecast.

A method for improving the performance of NWP models is the use of an ensemble approach (Gneiting & Raftery, 2005; Zhang & Pu, 2010; Lee et al., 2012; Bauer et al., 2015). This approach consists in repeating simulations under same initial and boundary conditions but varying the physics scheme parametrization each time. This parametrization typically includes: radiative transfer, vegetation and soil characteristics, microphysics, and flux interaction of heat, moisture and momentum in the soil/atmosphere interphase, among others. Ensembles performance have been widely used by different authors (Ruiz et al., 2010; Evans et al., 2012; Kim et al., 2013; Katragkou et al., 2015; Ekström, 2016) for capturing climate projections uncertainties, or achieving an optimal physics scheme parametrization. On the other hand, forecasting models are in general very dependent on the local condition (i.e. topography, hydrology, time of year, etc.). To overcome this issue, an iterative testing exploring different parameters' values is a suitable tool for knowing which parameters need to be specified and investigated with greater accuracy (Hirabayashi et al., 2011). Furthermore, a realistic model performance cannot be attributed to the achievement of a single scheme parametrization. Due to the complexity and non-linearity of atmospheric equations, the totality of the schemes parametrizations are involved in the output performance.

Another issue commonly tested for rainfall prediction over big watersheds is the forecast lead-time, or the time prior to the forecast date. An appropriate lead-time can considerably enhance the simulation accuracy. Rainfall forecast performance is sensitive to the temporal and spatial scale, becoming worse with lead-times longer than 5 to 6 days, and eventually meaningless after 9 days (Siddique et al., 2015). Advances in NWP have made lead times of 2 weeks feasible (Buizza & Leutbecher, 2015), but forecast is more reliable for shorter lead-times, i.e. 3 days, for lighter rainfalls within bigger basins (Siddique et al., 2015). Hence, a rainfall forecast in a small watershed for heavy rainfalls is a challenge, even when shorter lead-times are considered.

Even though many studies using the Weather Research and Forecasting (WRF) model (Skamarock et al., 2008) have already embraced its limitations over complex topography (Jiménez et al., 2010; Zhang et al., 2013; Karki et al., 2017; Soltanzadeh et al., 2017; Jiménez-Esteve et al., 2018), few studies have focused on the South American Andean mountainous region. WRF was used over the Nahuelbuta Mountains, in coastal southern Chile ($37°$S - $38°$S), to successfully simulate observed data seasonal and daily mean rainfall distributions Garreaud et al. (2016). WRF was also used to study the direct effect of the Andean topography on wind speed and direction over the Argentinian foothill (Mendoza) Puliafito et al. (2015). Finally, WRF was used to forecast urban PM_{10} and $PM_{2.5}$ pollution events over Santiago's foothill, but their physical scheme combination did not comprise any representation of rainfall events Saide et al. (2011). They only briefly discussed the modeling of the coastal lows development into Santiago's valley. On the other hand, the Chilean Meteorological Agency (DMC in spanish) performs daily WRF simulations with a physics scheme calibrated to predict weather in Chile Central Valley, a 1200 Km length region, which barely captures the Andean mountain and foothill topography. This simulations are made using a 6 Km horizontal resolution and 50 vertical levels, more densified in the top and bottom boundaries.

The objectives of this work are to study and test different WRF configurations and physic processes parameterizations for the forecasting of rainfall over mountainous regions, as well as to test the effects of different lead-times. The performance of the WRF simulations is evaluated according to their ability to represent relevant characteristics of the temperatures dynamics and rainfall events for the prediction of floods (i.e. length, peak intensity, concurrent freezing level and the N-rainiest hours) over the Andean front range in central Chile, particularly, the Quebrada de Ramón catchment, a small basin located in the area. In our analysis we used three storm events of different characteristics that took place between 2015 and 2017. The outline of this study is as follows: Section 2 describes the rainfall events selected for this study. Section 3 presents WRF configuration, grid resolution, physical ensemble options, lead-times, and sensibility studies. In Section 4 the results and discussion related to the optimal physical scheme are presented. Final conclusions are presented in Section 5.

2. CASE STUDY

2.1. Field Data

The case study area corresponds to the Quebrada de Ramón basin, a 36 Km^2 mountainous watershed located in central Chile whose highest elevation is 3250 m. Its complex and steep topography has a maximum elevation gradient of 220 m per 1 Km and a high average slope ($\sim$ 38%) (Catalán, 2013). Its outlet is located at an elevation of 800 m, in the east part of Santiago, the capital of Chile. The urban dynamics in this area neither considered high return period flows nor detrital floods. A clear example of the consequences took place in May 3^{rd} 1993, when a warm storm produced large floods and landslides in this and other front range basins nearby (Garreaud & Rutllant, 1997). The flood injured 3500 people and caused 50 human losses. The situation was aggravated by the presence of houses located in the piedmont and the floodplains (Vargas, 1999).

Santiago (33°30'S; 70°42'W) is representative of a semi-arid Mediterranean climate: warm temperatures with dry summers, a mean annual precipitation of 310 mm and ~ 26 rainy days per year. The rainy season (april - september) groups about 91% of the annual precipitacion, specially between June to July, months in which nearly half of the annual precipitation takes place (Dirección General de Aeronáutica Civil (DGAC), 2018). This general weather pattern has remained constant over time, since no trends were found on monthly rainfall, mean and maximum anual precipitacion for the period 1950-2018 using the Mann-Kendall test (Mann, 1945; Kendall, 1975) with a 5% significance level.

For this study, data were collected from the Apoquindo meteorological station, located nearby Quebrada de Ramón's centroid (33°26'S; 70°28'W) at an elevation of 1625 m.a.s.l. Six meteorological variables are registered every 10 min: temperature, relative humidity, solar radiation, wind speed and direction, and rainfall (Figure 2.1). Moreover, hourly and daily precipitation and temperature data were obtained from 13 meteorological stations located in Santiago and its surroundings were used to verify the orographic gradient and to analyze the return period of the storms events (Table 2.1).

TABLE 2.1. Meteorological stations names, coordinates and recorded variables: T (air temperature) and P (precipitation). Stations located inside Santiago are indicated with *

Name	ID	Latitude	Longitude	Elevation (m.a.s.l.)	Variables
San José Guayacán	SJ	33°37'S	70°21'W	928	Hourly T, P
Apoquindo	AP	33°27'S	70°28'W	1625	Hourly T, P
Quebrada de Macul *	QM	33°30'S	70°31'W	950	Daily T, P
Antupirén*	AN	33°30'S	70°31'W	904	Daily P
Cerro Calán*	CC	33°24'S	70°32'W	904	Daily T, P
Tobalaba*	TO	33°27'S	70°33'W	650	Daily T, P
La Platina*	PL	33°34'S	70°38'W	630	Hourly T, P
Quinta Normal*	QN	33°27'S	70°41'W	534	Daily T, P
Lo Pinto*	PI	33°16'S	70°44'W	512	Hourly T, P
San Pablo*	SP	33°27'S	70°45'W	490	Hourly T, P
Pudahuel	PU	33°24'S	70°48'W	482	Daily T, P
Rinconada de Maipú	RM	33°30'S	70°51'W	462	Hourly T, P
Hacienda Lampa	HL	33°17'S	70°51'W	493	Hourly T, P
El Paico	PA	33°42'S	70°60'W	275	Hourly T, P

The freezing level location (i.e. a elevation representative of the snow line that controls the spatial occurrence of rain and snow) was obtained from the Santo Domingo atmospheric sounding station record (available on http://weather.uwyo.edu/upperair/sounding .html). Soundings are made twice a day (00Z and 12Z) at 105 km from the city of Santiago (33°65'S; 71°61'W). These measurements are considered to describe Santiago atmosphere's features, as the city is located within the area of measurements' representativeness defined by a 150 km radius, based on the negligible effects of topography and near coast interactions in the upper atmosphere (Roney, 2007).

2.2. Meteorological characterization of rainfall events

For the the scheme parameterization and calibration of WRF, we considered three rain events: a frontal system rainfall (19^{th} October 2015, hereafter refered to as OCT15), a cutoff

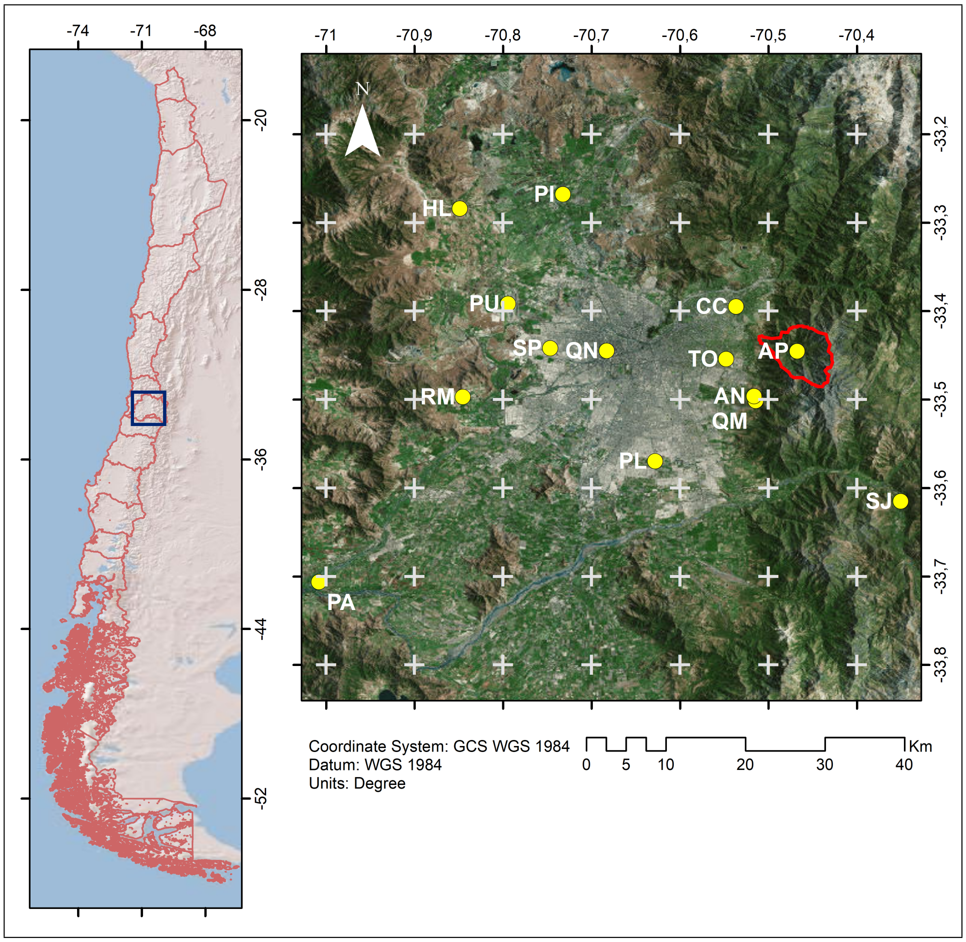

FIGURE 2.1. The Quebrada de Ramón's basin (outlined in red), in Santiago de Chile's piedmont, and the location of Apoquindo meteorological station and the other 13 meteorological station in Santiago's valley and foothills.

low rainfall (17^{th} April 2016, hereafter refered to as APR16) and a hybrid between cutoff low and frontal system rainfall (11^{th} May 2017, hereafter refered to as MAY17). Cutoff lows are meteorological phenomena that take place in medium to high latitudes (20°S - 40°S), more likely during autumn and winter (i.e. from April to September) (Fuenzalida et al., 2005; Garreaud & Fuenzalida, 2007). They can cause extreme cold weather and precipitation in high elevations above 1000 m, coupled with strong winds and occasional thunderstorms (Aguilar, 2010). These three rainfall events are considered to be representative of the possible range of rainfall events in this region.

Meteorological forcing data was obtained from NCEP/NCAR Reanalysis (NCEP: National Center for Environmental Prediction & NCAR: National Center for Atmospheric Research). In this study we use the period 1981-2010 for computing the mean anomalies during the studied rainfall events. An anomaly shows the difference of any meteorological variable from its long-period mean value for a given location. For wind velocity vector, the absolute value of the anomalies is obtained from u and v, the zonal and meridional wind velocity, respectively. (See Appendix C, Eq. C.1).

2.2.1. 19^{th} October 2015 rainfall event (OCT15)

Between October $16^{th} - 20^{th}$ 2015 (largest intensities between 19^{th} October 2015 1100 UTC and 20^{th} October 2015 0000 UTC), Chilean central valleys were affected by an event that left a relatively high precipitation over the mountainous region (i.e. 46 mm in the Apoquindo gauge vs 21 mm in Quinta Normal station, Table 2.1), whose rainiest hour had a return period of 2.3 years according to the Quinta Normal records. This event was caused by a cutoff low developed in the oceanic zone ($80° - 90°$ W and $30°$ S, Figure 2.2), which produced a nucleus of negative anomalies in the 500 hPa geopotential level, with a magnitude of -150 m. The event was intensified by the jet stream at 250 hPa, with its nucleus of largest intensities (30 m/s positive anomalies) located just above the Chilean central region ($30°$ S, Figure 2.2).

2.2.2. 17^{th} April 2016 rainfall event (APR16)

In April $15^{th} - 17^{th}$ 2016 (15^{th} April 2016 0900 UTC to 17^{th} April 2016 2000 UTC), an extreme rainfall event affected Chile's central region. On April 17^{th}, 108 mm of rainfall were measured at the Apoquindo meteorological station in 24 hours. According to Quinta Normal historical records, the maxmium hourly rainfall of this event had a 46 years return period, even though the acummulated rainfall of 14 hours within the storm peak had a return period of 10 years (MOP, 2013).

The frontal system moved from north to south, with negative anomalies in the atmospheric pressure and geopotential height at 500 hPa (-150 geopotential meters). At the same

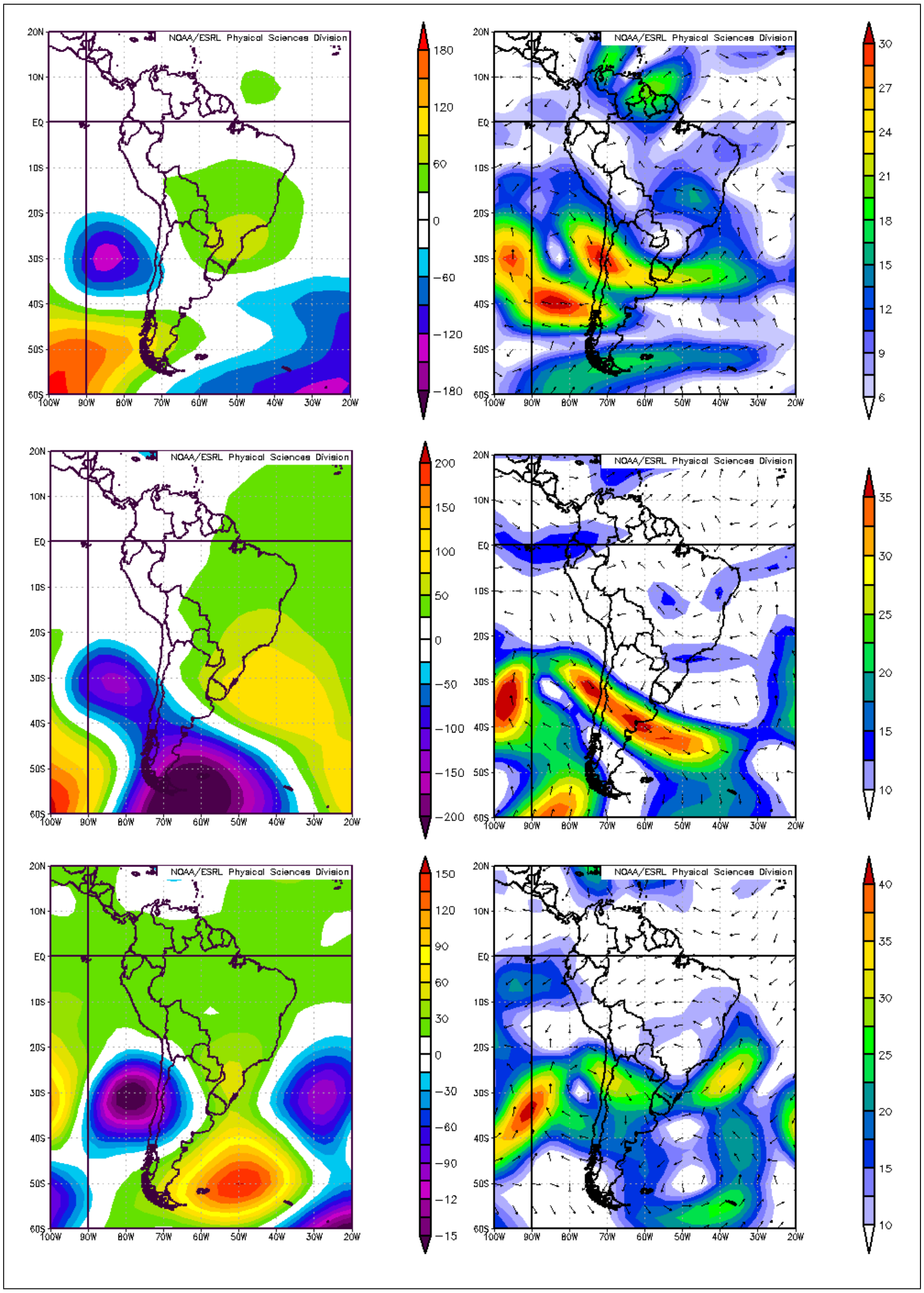

FIGURE 2.2. NCEP/NCAR Reanalysis composite anomaly for **OCT15** (upper row), **APR16** (middle row) and **MAY17** (bottom row) events, for 500 mb geopotential height (m) (left column) and 250 mb vector wind (m/s) (right column)

time, an intensification of both subtropical and polar jet streams took place at 250 hPa, allowing higher wind intensities in the system nucleus (positive anomalies of 35 m/s in the wind vectors) (Figure 2.2), favoring the cloudiness development over central Chile.

Satellite images showed a significant moisture contribution, advected from lower latitudes, which incorporated more precipitable water into the system (Figure D.2, Appendix D). This quasi-stationary weather front led to a warm winter storm, allowing more rainfall to precipitate over central Chile. During most part of a warm storm, precipitation is caused by mechanical uplift of moist air over the Andes, developing its maximum precipitation in mid-elevations inlands. This behaviour is consistent for several warm storms in other world regions, where heavy rainfall and flood events happen (Garreaud, 2013).

Additionally, the freezing level was above 3000 m, causing a large contribution of liquid precipitation at relatively high temperatures. In fact, during April 16^{th}, the Mapocho river in Santiago's basin, flooded the central part of the city, where a riverbed modification due to a construction took place. Because of its large duration, maximum intensity and total amount, this rainfall event was used for initial WRF modifications over the grid discretization, land use and initial and boundary condition data.

2.2.3. 11^{th} May 2017 rainfall event (MAY17)

With 53 mm of rainfall recorded in Apoquindo station in two days, the event of 11^{th} May 2017 0400 UTC to 12^{th} May 2017 0100 UTC affected a large portion of Chile. This event corresponds to a return period of 3 years in Quinta Normal hourly records. In the previous days, the system presented a trough with closed circulation at 500 hPa, a typical cutoff low characteristic. Additionally, the jet stream at 250 hPa had a strong zonal direction in the trough posterior part (Figure 2.2).

During the rainfall event, a low pressure center on the surface associated with the weather front was observed. At higher elevations, the typical cutoff low pattern was not visible, as there was no clear closed-circulation and the jet stream was coupled to westerlies. At 500 hPa the trough contributed with additional divergence, generating more cloudiness over the affected area.

3. MODEL CONFIGURATION AND IMPLEMENTATION

3.1. Initial and boundary condition data

ARW-WRFv3.5 (Skamarock et al., 2008), a state-of-the-art mesoscale NWP model was used in this work. The model is suitable for a wide range of applications, such as weather routine forecast, research simulations, and evaluation of parameters in simulated systems. WRF solves the scalar conservation and compressible non-hydrostatic Euler equations, through vertical coordinates (η levels) with a variable grid density. WRF system is supported and maintained by NCAR (http://www.mmm.ucar.edu/wrf/ users).

Meteorological forcings according to the NCEP operational Global Florecast System (GFS) and the NCEP Final Operational Global Analysis data (FNL) were initialy compared. GFS is composed of four blocks (atmosphere, ocean, land/soil and sea/ice), providing a $0.25°$ resolution grid with the forecast of atmospheric and land-soil variables every 3 h for modeling periods after 2015 (http://rda.ucar.edu/datasets/ ds084.1/). Operational forecasters, as the DMC in Chile, use GFS as boundary condition to simulate precipitation at finer resolution via NWP. On the other hand, FNL is a $1°$ resolution gridmap produced every 6 h, prepared approximately an hour after GFS started, which allows more observational data to be used ($\sim 10\%$) in the upgrade of initial and boundary conditions. FNL data are available for periods after 1999 (http://rda.ucar.edu/datasets/ ds083.2/). Finally, sea surface temperature (SST) at a $0.5°$ resoultion from the NCEP SST analyses database were also provided to the WRF model.

The forecasts were carried out with a 32 cores machine (2.30 GHz Intel Xeon E5-2698 v3), taking less than 5 h to retrieve operational daily forecasts at a resolution of 6 Km. This time considers 1 h in data preparation and downloading of initial and boundary conditions, (GFS $0.25°$ for DMC forecasts), 2.5 h in running WRF and 45–60 min in post-processing.An initial testing over GFS/FNL meteorological forcing considered three different lead times for APR16 event (i.e, 120, 96 and 72 h): although both dataset performed similarly, the rainfal total length provided by GFS was more feasible. Thus, only GFS dataset was used in the simulations (See Appendix G.3. for a complete study of both datasets combined with variable lead times).

3.2. Simulation domains and topography complexity

The domain of the WRF simulations was composed of three nested grids with 54, 18 and 6 Km of resolution. These were based on a Lambert Projection centered at Santiago de Chile, interacting with each other through a two-way nesting strategy (Figure 3.1). The biggest or parent domain (d01, 54 Km) covered South America western region, the Pacific and part of the Atlantic Ocean. The first nested domain (d02, 18 Km) embraced Chilean and Argentinian central regions and the Pacific Ocean near the shore. The innermost domain (d03, 6 Km), main focus of this study, covered a reduced portion of the Pacific Ocean, central Chile and the Andes mountains.

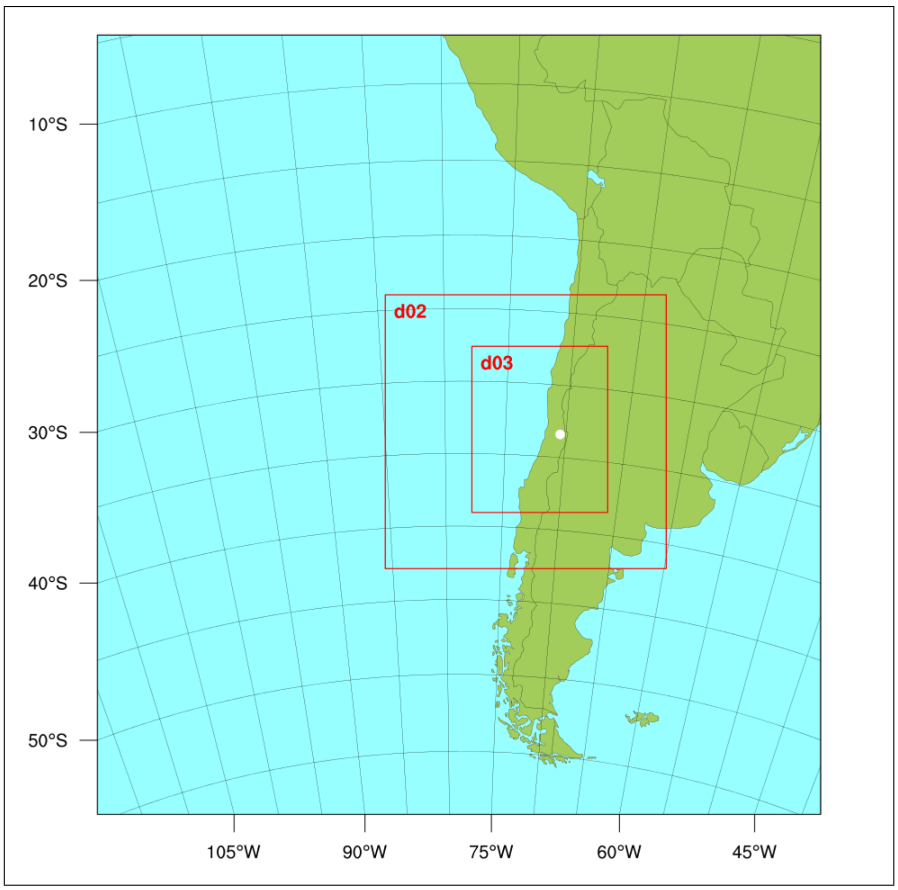

FIGURE 3.1. WRF model domains for all the simulations. Domain d01 correspond to the whole plot, and the white point is over Santiago, Chile

WRF can numerically diverge with high elevation gradients, resulting in anomalous vertical wind speeds with gradients of ~ 300 m per 1 Km (Otarola et al., 2016). Moreover, due to the model grid resolution, the complex topography produced a considerable overestimation of Apoquindo station's elevation ($+314$ m) (See Appendix E, Figure E.1). Following the approach by Carvalho et al. (2012), the Apoquindo station location in WRF was moved within a 5 km radius. The best output location to represent the station was 5 Km further north of its real location, which produced a height underestimation of 200 m, but a better performance of the rainfall temporal distribution (not shown).

3.3. WRF resolution and physics schemes

Initial testing over the APR16 event were made focused over (1) two vertical level resolutions, (2) two land use and three land surface models. Results from these initial simulations allowed the definition of the final schemes parameterization and grid resolution, which was used in a final set of simulations to test different MP schemes and lead times.

3.3.1. Vertical levels

The prediction of the microphysics and PBL processes, and thus the rainfall, is expected to improve with a finer vertical grid resolution. However, doubling the number of vertical levels from 31 to 62 did not enhance quantitative precipitation forecasts in the central US (Aligo et al., 2009). Based on the studies from Seaman et al. (2009) and Rahn & Garreaud (2010), Saide et al. (2011) proposed an optimal density of 39 vertical levels in the study region, with a first layer at 10 m and six levels below 100 m, which allowed the best forecasting of wind speed, temperature and chemical compounds concentrations. This discretization was compared against one with 50 vertical levels currently used by DMC (See Appendix F for more details). This finer discretization reproduced temperature profiles and the saturated atmosphere near surface more acurately, and thus it was chosen as the default discretization for the following simulations (See Appendix G.1).

3.3.2. Radiation and Cumulus scheme physics

Short and long wave radiation schemes determine radiative fluxes in the simulation. The Dudhia short wave scheme (Dudhia, 1989) and the RRTM long wave radiation scheme (Mlawer et al., 1997) were chosen due to their consistent performance according to Saide et al. (2011). On the other hand, cumulus schemes simulate the sub-grid processes related to convective clouds. Given the WRF capacity to explicitly solve this, a parameterization is not needed in the inner domain. In the external domains, the Grell 3D Ensemble (Grell, 1993) was used because of its acceptable performance when simulating convective rainfall.

3.3.3. Land Use, Land Surface Model and PBL

WRF's Land Use (LU) for terrain characterization uses different categories to depict landscapes, crops, vegetation, forests, and urban areas. WRF versions after 3.1 provide a Land Use dataset obtained from 2001 Moderate Resolution Imaging Spectroradiometer (MODIS) satellite products. On the other hand, the U.S. Geological Survey (USGS) provides an alternative dataset of land-cover classification, as recent studies have found that WRF terrain representation may be inaccurate (Cheng et al., 2013). However, Saide et al. (2011) compared both LU dataset and found that the USGS underestimates the extension of Santiago area, probably due to the use of old maps. Hence, MODIS data were chosen for further simulations.

Land Surface models (LSM) calculate heat and moisture fluxes above the land, sea and ice cover. The simplest LSM physics option that considers a 5-layer model for thermal diffusion was not considered, as it neither includes vegetation effects, nor the changes in snow cover, or soil moisture over time. Soil moisture is the most significant part of flux exchanges between the surface and the first level of the model, and also a crucial factor that affects near surface temperature and wind (Dimitrova et al., 2016). Other LSM options include, Noah LSM, which is broadly recommended for capturing the heterogeneity in surface heat fluxes (Ek et al., 2003), and Noah-MP LSM, which provides a more accurate simulation of snowmelt and the diurnal variations of the snow surface temperature, snow cover fraction and surface emissivity. Nevertheless, Noah-MP was finally chosen given the improvements to the simulation of surface fluxes, timing of snow water equivalent and runoff peaks (Niu et al., 2011). (See Appendix G.2. for detailed testings results).

The PBL scheme determines surface heat and moisture fluxes due to eddy transports in the remaining volume of the atmospheric column over the terrain. In this study, the Mellor-Yamada Nakanishi Niino (MYNN) Level 2.5 was used as a local approach with total kinetic energy (TKE) closure (Nakanishi & Niino, 2006). Note that Saide et al. (2011) used the same scheme because it was numerically more stable. Overall, MYNN performs better due to a good vertical profiles' representation, which in turns produces a closer agreement with the planet boundary layer shape, magnitude and maximum values. PBL was not tested in this study, as large-scale phenomena have more influence over the total rainfall amount than small-scale eddy effects nearby surface during an extreme precipitation event. Finally, for compatibility reasons with the PBL scheme, MYNN includes the MYNN Surface Layer (SL) option.

The final WRF configuration is summarized in Table 3.1, for which 50 vertical levels of vertical resolution are applied together with the GFS dataset.

TABLE 3.1. Final WRF simulation schemes

Physical scheme	Parametrization
Short-wave radiation	Dudhia
Long-wave radiation	RRTM
Cumulus	Grell 3D Ensemble
Planet Boundary Layer	MMYN 2.5
Soil Layer	MMYN
Land Surface Model	Noah-MP

3.3.4. Microphysics

Microphysics (MP) schemes explicitly resolve processes of water, cloud and precipitation, and their mixed-phases (i.e. ice-water interaction).The Lin et al scheme (hereafter referred to as LIN) employs six forms of water (water vapor, cloud water, cloud ice, rain, snow and graupel). Moreover, this scheme allows the explicit inclusion of snow, and the correct simulation of changes from cloud ice to snow and then to graupel. In general, LIN better describes the dynamics of the clouds inner processes (Lin et al., 1983), being appropriated for high resolution simulations.

The WRF-Single-Moment-Microphysics scheme (WSM) varies according to the class, i.e. the number of prognostic water substance variables. The WSM 3-Class (hereafter referred to as WSM3), used in the DMC initial forecast, contains water vapor, cloud water/ice, and rain/snow. In this scheme rain and water occur above the freezing level, and snow and ice below it. On the other hand the WSM 6-Class (hereafter referred to as WSM6) contains mixing ratios of water vapor, cloud water, cloud ice, snow, rain and graupel, and thus is more appropriate for high resolution simulations. Although both WSM schemes have similar behaviors when simulating extreme rainfalls at low grid resolutions (~ 45 Km), total rainfall and maximum intensity are better simulated in WSM6 at finer resolutions (~ 5 Km) (Hong & Lim, 2006). Moreover, for extreme rainfalls, the combined effect of microphysics and ice sedimentation (available in LIN and WSM6) provides a better representation of cloud covered areas, mean temperatures in the upper troposphere and surface rainfall amounts (Caneo, 2010). Nonetheless, in this study, we tested the LIN, WSM3 and WSM6 schemes.

3.3.5. Lead time

Forecast accuracy depends not only on the parameterization of physical schemes and grid resolution, but also on the lead time. Commonly, forecasts get worse with increasing lead time, because synoptic characteristics are constantly changing. A smaller outer domain and shorter lead times allow more accurate rainfall simulations, whereas larger domain sizes and lead times can increase inner variabilities in WRF, displacing the spatial rainfall band and affecting rainfall forecasting (Sikder & Hossain, 2016). Although acceptable precipitation forecasting can be obtained with lead times up to 6 days, values of 3 days or less produce much better results (Siddique et al., 2015). In this study, lead times of 3, 4 and 5 days (72, 96 and 120 h) previous to the day with the maximum rainfall intensity were analyzed.

In summary, the final WRF configuration depicted in Table 3.1 will be used to test 3 MP parameterizations and 3 lead times. All the MP parameterizations are considered for the APR16 event, but only the LIN and WSM6 parameterizations will be used in the OCT15 and MAY17 events, given their more specific depiction of water phases.

3.4. Model validation

Observed data from the Apoquindo and other stations located in Santiago valley and piedmont (Figure 2.1) were used to assess the quality of the meteorological simulations. Note that this assesment excludes the first day of all the simulations, used for warming up the model (*spin-up* period). Simulated temperature and rainfall time series were assessed via the mean absolute error (MAE), a robust metric that prevents single events from having a large impact on the statistic (Ekström, 2016).

$$MAE = \frac{1}{N}\sum_{t=1}^{N}|S_t - O_t| \tag{3.1}$$

where *N* is the total number of data, and S_t and O_t are the simulated and observed meteorological data. In addition, we also use the concept of error, which corresponds to the difference between S_t and O_t at any time *t*. Finally, the simulations' performance was also characterized through the Nash-Sutcliffe Efficiency coefficient (NSE):

$$NSE = 1 - \frac{\sum_{t=1}^{N}(S_t - O_t)^2}{\sum_{t=1}^{N}\left(O_t - \bar{O}_t\right)^2} \tag{3.2}$$

NSE ranges [-∞, 1], where values larger than 0 imply a prediction better than the average of the observations ($\bar{O}$). Since the NSE is extremely sensitive to outlier data, a modified version of the Index of Agreement (IoA) (Willmott et al., 2012), is also used. IoA is a less sensitive to outliers metric that ranges $[-1,\ 1]$. Values bigger than 0.8 are considered to indicate a good performance of the model.

$$IoA = \begin{cases} 1 - \dfrac{\sum_{t=1}^{N}|S_t - O_t|}{2\sum_{t=1}^{N}\left|O_t - \bar{O}_t\right|} & \text{if } \sum_{t=1}^{N}|S_t - O_t| \leq 2\sum_{t=1}^{N}\left|O_t - \bar{O}_t\right| \\ \dfrac{2\sum_{t=1}^{N}\left|O_t - \bar{O}_t\right|}{\sum_{t=1}^{N}|S_t - O_t|} - 1 & \text{in other case} \end{cases} \tag{3.3}$$

The difference between simulated and observed wind directions in degrees (S_t^{Θ} and O_t^{Θ}) is obtained as follows. Note that positive values of $S_t^{\Theta} - O_t^{\Theta}$ represent an anti-clockwise deviation.

$$S_t^{\Theta} - O_t^{\Theta} = \begin{cases} S_t^{\Theta} - O_t^{\Theta}\left(1 - \left(\frac{360°}{\left|S_t^{\Theta} - O_t^{\Theta}\right|}\right)\right) & \text{if } \left|S_t^{\Theta} - O_t^{\Theta}\right| > 180° \\ S_t^{\Theta} - O_t^{\Theta} & \text{in other case} \end{cases} \tag{3.4}$$

S_t^{Θ} is calculated as shown in Appendix C. Finally, we adopted the tolerance criteria for absolute error, defined in Table 3.2, used by DMC.

TABLE 3.2. Absolute difference tolerance criteria for simulated variables used by DMC

Meteorological variable	Absolute difference tolerance criteria
Dew temperature	1°C in surface, 2°C in atmosphere
Temperature	1°C in surface, 2°C in atmosphere
Wind speed	2.57 m/s (~ 5 knots) for all data
Wind direction	20° in surface, 15° in pressure levels above the 850hPa

Non-zero hourly simulated rainfall pulses were assumed to be those larger than 1 mm, while an inter-event arrival time (IEAT) (i.e., the minimum dry time between two independent rainfall events) of 30 hours recommended for Santiago (Zegpi & Fernández, 2010) was adopted. To assess the temporal distribution of the most intense portion of the rainfall event, the N-rainiest consecutive hours (NRH) were computed. Temperatures time series associated with each NRH (T_{NRH}), were analyzed via MAE, emphasising both precipitation and temperature when N=5 h (i.e. NRH(5) and $T_{NRH(5)}$). This time corresponds to the estimated time of concentration of Quebrada de Ramón, a metric that is representative of the hydrological response time of the catchment.

4. RESULTS

4.1. Local Conditions

To assess the local performance of WRF over the rainfall events, we first characterized the overall rainfall orographical gradient using total rainfall amounts registered in all the meteorological stations (Table 2.1). Figure 4.1 compares total simulated rainfall amounts (considered to be the mean of the values simulated using the three lead times for every MP option) against the observed ones. Different markers according to the elevation are used in the figure. The left panels compare in every meteorological station simulated and observed data, and the dashed line corresponds to the 1:1 ratio. The right panels plot rainfall against height; the scatter in the plots represents simulated values for several locations in Santiago and the west hillslope of the Andean foothills, to give a spatial context for the WRF rainfall distribution.

For the OCT15 rainfall event (Figure 4.1, upper row) WRF overestimates rainfall amounts, particularly at higher elevations. The orographical gradient inside Santiago city is accuratelly simulated, but the scatter plot shows more dispersion at elevations higher than 700 m.a.s.l. (i.e., the mountainous area of Santiago). The LIN MP option produces a bigger bias than the WSM6 option for all the points belonging to the Santiago basin, although this bias is reduced for lower elevations. In general, WRF predicts more rainfall with larger latitudes. Overall, the WSM6 schemes provides better results (i.e., less biased).

In the APR16 event (Figure 4.1, central row), WRF overstimate rainfall amounts for all the stations located above 800 m.a.s.l., corresponding to Santiago's foothills. Predictions for lower elevations are much better, with small underestimations of the observed precipitation. WRF simulates a strong correlation between total precipitation and height, although the observed rainfall ranges between $80 - 120$ mm. In the orographical gradient, rainfall was undestimated in the west part of Santiago (lower elevation) and overestimated in the foothills. The scattered pattern appears once more, with more dispersion (and thus, bigger biases) for the foothill stations located in the southern area of Santiago (AN, QM, and SJ stations). This also happened for the Apoquindo station, where a ~ 100 mm bias was simulated. The bias reduces for gauges located at northern latitudes below 1000 m.a.s.l. (gauges CC and TO).

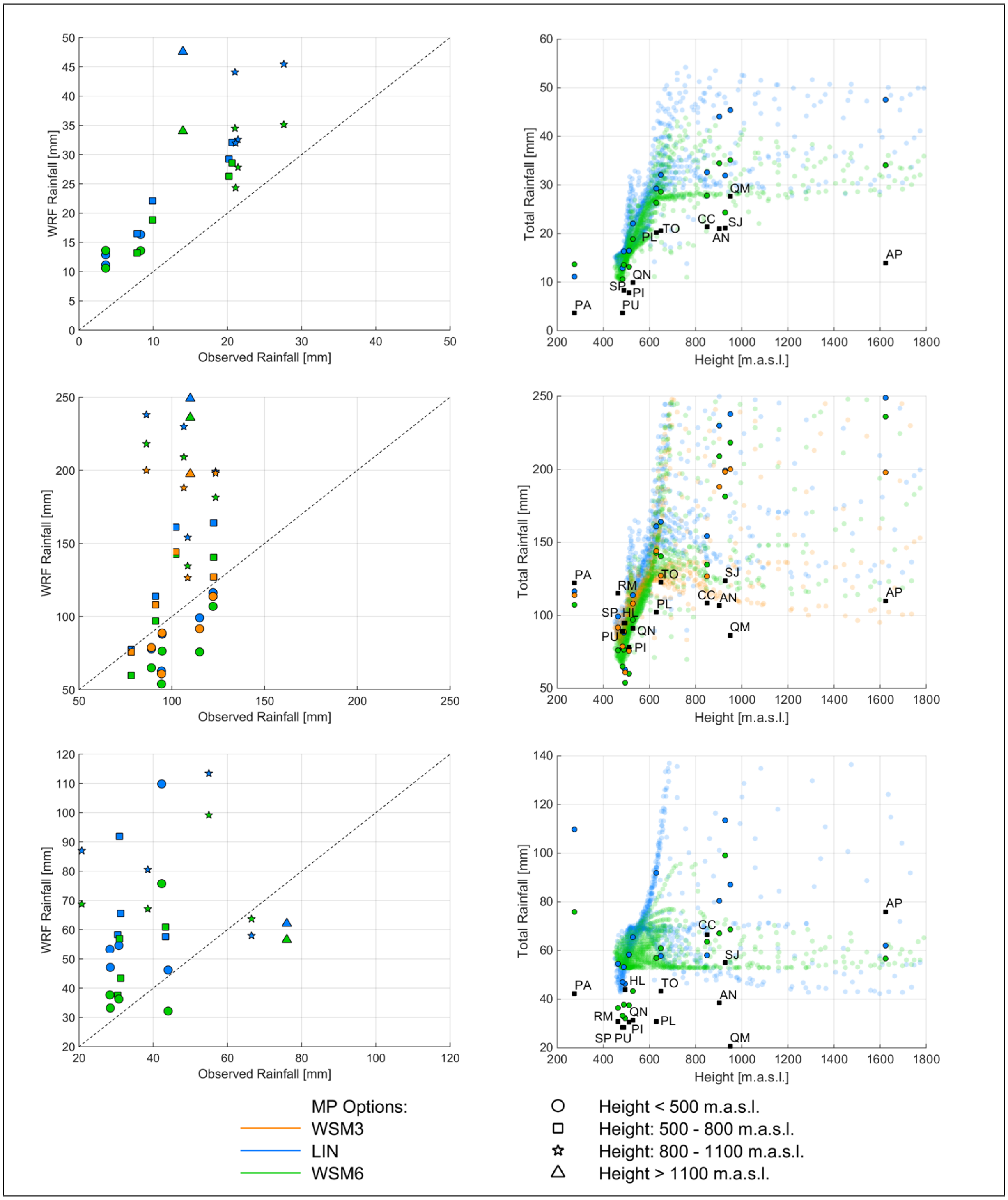

FIGURE 4.1. Total observed and simulated precipitation according to height (left) and orographical gradient (right) for OCT15 (upper row), APR16 (central row) and MAY17 (lower row) events. The mean value of all lead times (72, 96 and 120 h) and three MP parameterizations (LIN, WSM6 and WSM3 where used) are considered. In right panels, observed data are plotted in black squares.

Overall, the LIN scheme produced the larger biases, whereas WSM3 and WSM6 performs similarly.

Finally, for the MAY17 event (Figure 4.1, bottom row), rainfall is overestimated particularly at higher elevations, although the rainfall in the highest two stations was undestimated by WRF. The smooth orographical gradient in the recorded data was captured in the WRF simulation. In Apoquindo station, both MP options (LIN and WSM6) produced similar bias (~ 20 mm). Once more, the WSM6 scheme performed generally better, as it produced smaller biases.

4.2. Rainfall and temperature simulation

The frontal system conditions of the OCT15 event allowed a more accurate prediction of the temporal distibution of the rainfall (IoA = 0.40 for the mean of LIN simulatons, and 0.44 for the mean of WSM6 simulations), since most MP schemes captured the initial rainfall (October 19^{th}). Simulations with 120 h of lead time also captured a previous pulse (October 17^{th}), as seen in Figure 4.2 (upper row). For shorter lead times, both MP schemes not only predicted the occurrence of another precipitation pulse (October 21^{th}), but also its magnitude, with a bias of less than 10 mm.

None of the simulations could accurately predict the APR16 rainfall event. There was a $\sim$ 48 h lag between the observed and simulated rainfall peaks (Figure 4.2, central row). Furthermore, for simulations with shorter lead times, a new rainfall pulse was predicted. Although this pulse matches the observed peak occurring in April 17^{th}, rainfall errors of ~ 200 mm are present all over the ensemble.

If the rainfall beginning is considered to be April 16^{th}, ignoring the first rainfall pulse of April 15^{th} (Figure 4.3), the model performance improves, with a smaller MAE (~ 1 mm) and a bigger mean IoA value for all MP options, although some values are still negative. A mean value for the three lead times considered shows a higher score in the WSM3 scheme (IoA = 0.48 against IoA = 0.39 for LIN and IoA = 0.30 for WSM6). If a lead time based analysis is made, the simulations with 120 h have the worst performance: LIN and WSM6 schemes have a negative IoA score, and the WSM3 schemes simulates IoA = 0.38. As the lead time decreases, the differences among schemes disminishes, resulting in a sligthly better score for LIN and WSM6 (IoA = 0.66 and 0.62) respectively, similar to the IoA = 0.59 value of WSM3 scheme. In Figure 4.3 this forecast enhancement can be seen, as the simulations with a 72 h lead time matches the rain intensities between the last hours of April 16^{th} and the April 17^{th} noon. Furthermore, those simulations also captured the final pulse, even delayed, in the last hours of April 18^{th}.

Overall, the hourly forecast of the last storm hours was slightly more accurate. As the OCT15 and MAY17 simulated events don't show these errors, they are not explained by the complex topography, but by the rainfall properties which seem to be maximized in the initial GFS dataset. This rainfall amount error was observed in all the meteorological stations of Table 2.1 (not shown). Indeed, the APR16 event had unique meteorological characteristics and a large magnitude, which could partially explain the errors in the prediction.

For the MAY17 rainfall simulations there is an uneven ensemble performance for both MP options (IoA ~ 0.55), as the total rainfall amount is overstimated with the longest lead time and underestimated with the shortest lead times (Figure 4.2, bottom row). However, all simulations capture the rainfall pulse of May 11^{th}. Errors of ~ -50 mm obtained for lead times of 72 and 96 h are not produced by the simulation with lead time of 120 h, which captures May 11^{th} rainfall pulse, specially with the WSM6 option.

For temperature time series, there is an accurate performance for the whole ensemble, since the temperature dynamics was captured for the OCT15 and MAY17 events with minor errors. The mean performance between both schemes was very similar, with IoA = 0.77 for the OCT15 event and IoA = 0.69 for the MAY17 event. Steep temperature increments are well captured by all simulations, but overlapping and disagreement appear just before the rain started (~ 1 day, from the last hours of October 18^{th} for OCT15, and from May 10^{th} for MAY17, and ~ 3 days, from April 14^{th} for APR16), where a general temperature decayment takes place. Temperatures are overestimated in OCT15 and MAY17 events, just before the storm peak (April 19^{th} for APR16 and May 10^{th} for MAY17). A constant underestimation between April 14^{th} - 17^{th} can be seen in APR16, where all schemes had a similar performance

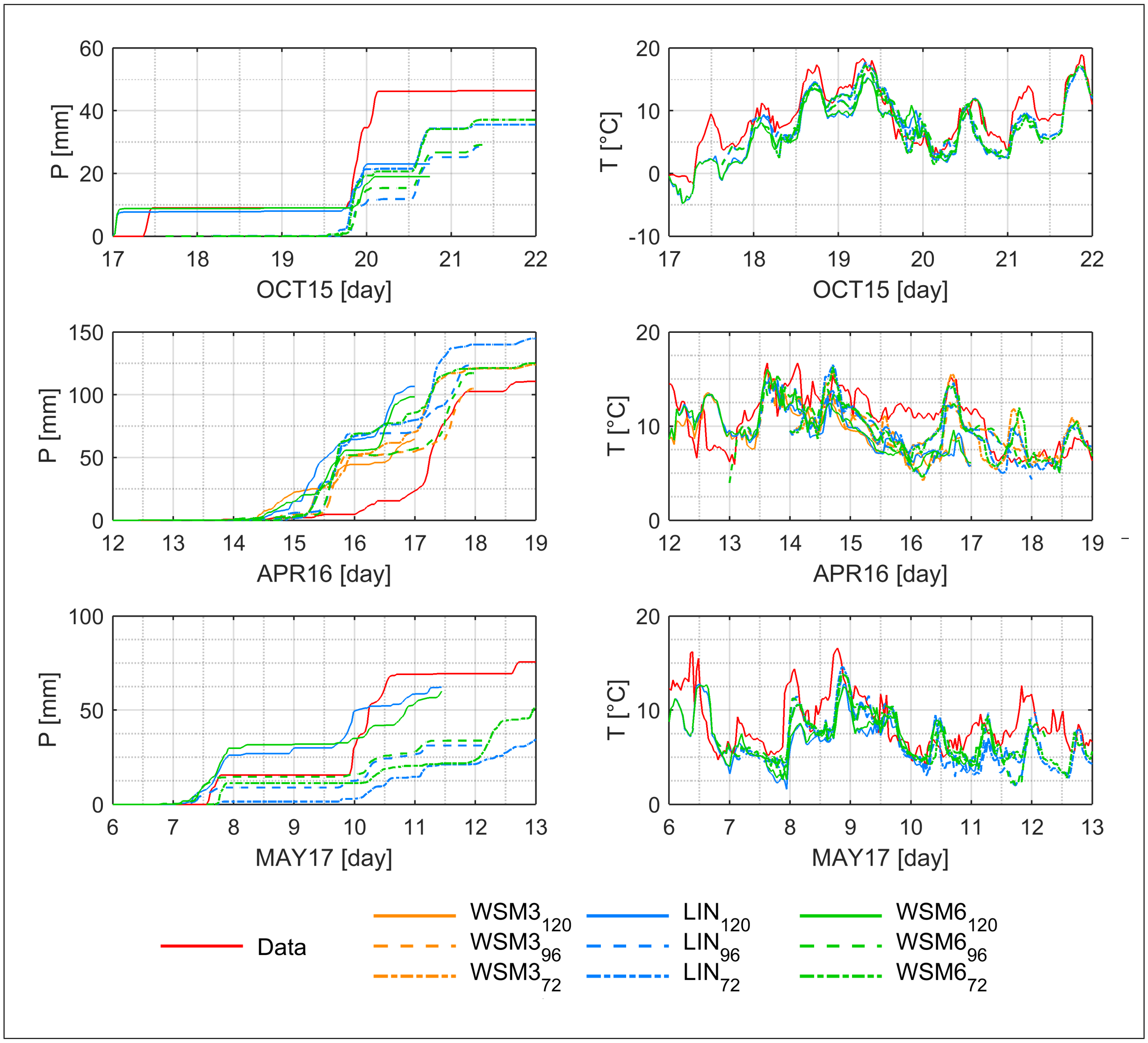

FIGURE 4.2. Observed and simulated precipitation (left) and temperature (right) time series for OCT15 (upper row), APR16 (central row) and MAY17 (lower row) events. Three lead times (72, 96 and 120 h) and three MP parameterizations (LIN, WSM6 and WSM3 where used) are considered.

(IoA ~ 0.47), probably due to the complex meteorological configuration of the event (Figure 4.2, right panels).

4.3. Rainfall forecast performance

In addition to the total rainfall amount and dynamics, another relevant attribute of precipitation events is the timing of the rainiest pulses. A good forecasting of this timing is essential

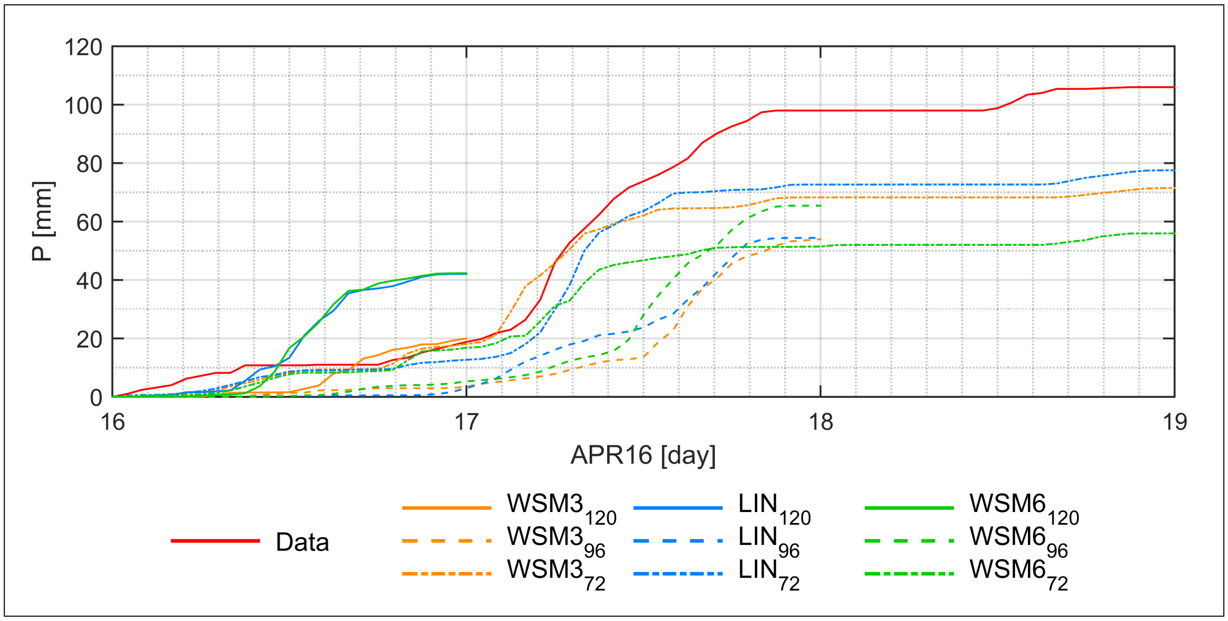

FIGURE 4.3. Observed and simulated precipitation time series for APR16 event, from April 16^{th}. Three lead times (72, 96 and 120 h) and three MP parameterizations (LIN, WSM6 and WSM3) are considered.

for modeling and predicting peak flows in a catchment of a given size. To visualize the performance of the forecasting on this regard, we plot the observed and simulated N rainiest hours (NRH) for all the different MP parameterizations and lead times, with N ranging between 1 and 10 h (Figure 4.4). Overall, the wide range of simulated curves contains the observed NRH curve, although major differences between the observed and simulated curves for the APR16 event were observed. NRH(5) values are ovestimated by all the ensemble. Unfortunatelly, the parameterization that best reproduce this value (WSM3_{120}) has the largest associated MAE value (Figure 4.4, central row and Figure 4.5, bottom row). Generally, the MAE of the T_{NRH} ensemble values were above the tolerance criterion shown in Table 3.2.

Observed and simulated NRH(5) are similar for the OCT15 and MAY17 events, with an underestimation of ~ 10 mm by the ensemble mean. Among the used MP schemes, WSM6 shows more consistency, regardless the lead time, and the errors are within the tolerance criterion for temperature (Table 3.2). LIN performs similarly, but results are less consistent and become worse with shorter lead times. Overall, the average WSM3 parameterization is the worst in reproducing NRH(5), while its relation with the lead time is less consistent than

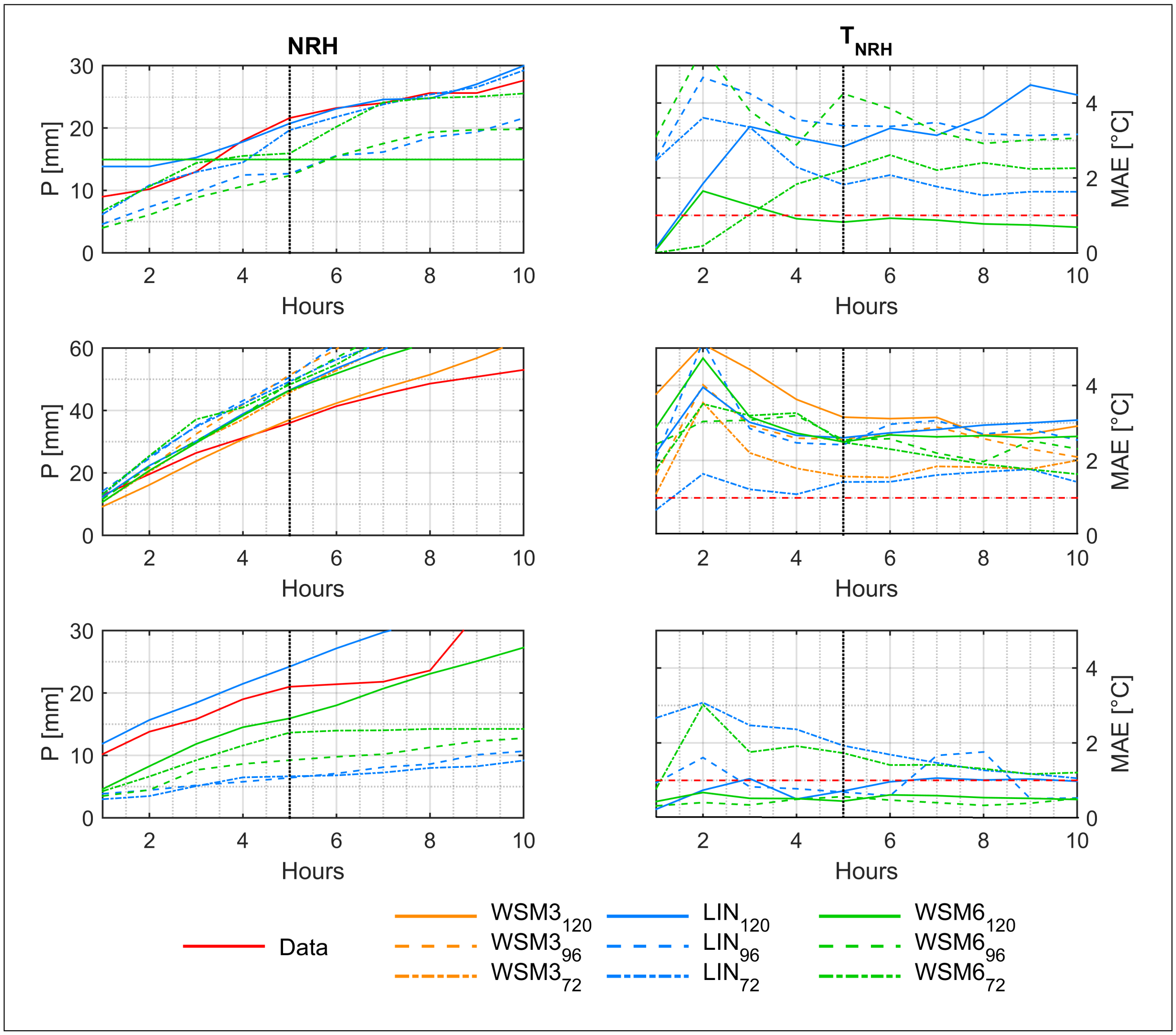

FIGURE 4.4. Observed and simulated N rainiest hours (NRH, left) and T_{NRH} MAE (right) from 1 to 10 hours, for OCT15 (upper row), APR16 (central row) and MAY17 (lower row) simulations. Vertical black dotted line represents Quebrada de Ramón time of concentration. Three lead times (72, 96 and 120 h) and three MP parameterizations (LIN, WSM6 and WSM3 where used) are considered.

the LIN and WSM6 MP options for NRH(5) and $T_{NRH(5)}$ MAE (see Appendix H, Figure H.6 for detailed results).

Total rainfall (Figure 4.5(A)) is clearly overestimated for the APR16 event, whereas for the other rainfall events, this amount is within the range of simulated values. These values tend to be better with shorter lead times, although no clear trend is observed. Furthermore, the average of the WSM6 simulations is worse than that of the LIN scheme in reproducing the

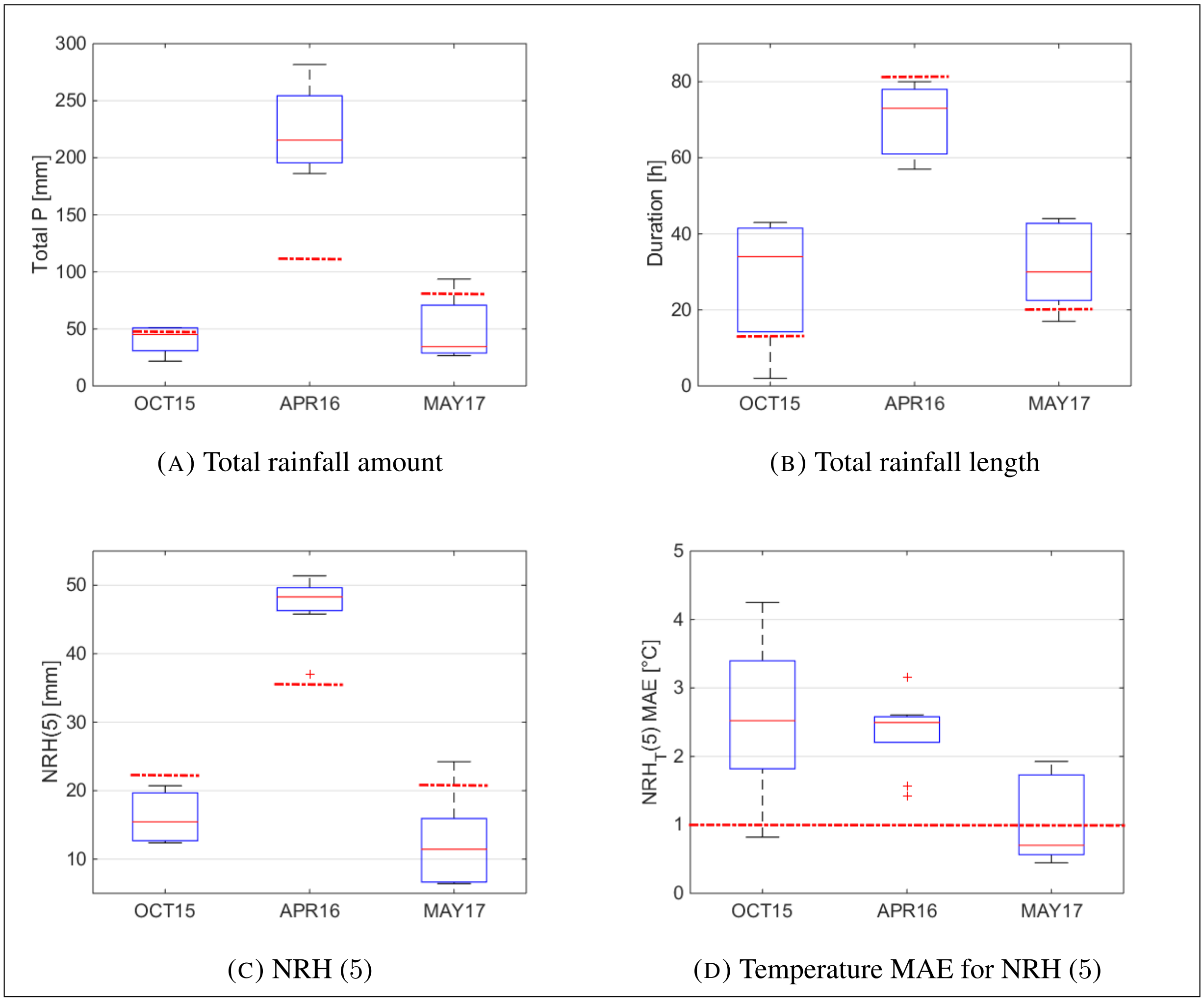

(A) Total rainfall amount

(B) Total rainfall length

(C) NRH (5)

(D) Temperature MAE for NRH (5)

FIGURE 4.5. Rainfall properties boxplots considering different MP parameterizations and lead times in the simulated ensembles. In panels A to C the observed value are plotted with a red dash dotted line; in panel D the red dashed line is threshold tolerance used by DMC for temperature bias (Table 3.2).

observed total amount (see Appendix H, Figure H.4 for detailed results). On the other hand, the rainfall length is reasonably predicted by the ensemble for all the events, with WSM6 performing better than the LIN parameterization, although real values are not within the 25^{th} – 75^{th} percentiles. Overall, and because it predicts the NRH(5) values, WSM6 is considered to be a good MP option to choose for rainfall forecasting in the study area, and eventually other frontrange catchments nearby (Figures H.4 and H.5 in Appendix H illustrate in more details this results).

4.4. Freezing level height

Freezing level height is quite well simulated by all the ensemble for the OCT15 and MAY17 events. Less differences between simulated and observed data are obtained during freezing level height declinements. On the other hand, when the freezing level height increases, the ensembles are more discrepant. Regardless of the behaviour of this level, during the rainfall peak the error tend to be negligible (Figure 4.6). For APR16, the declinement of the freezing level is overestimated, specially for longer lead times. This illustrates how the atmosphere stability development during cutoff low events is better captured using small lead times.

Shorter lead times improve the forecast of the OCT15 and MAY17 events, better capturing the freezing level increase ~ 2 days before the peak intensity (Figure 4.6). Longer lead times could not accuratelly simulate this peak value. A lead time of 72 h (3 days) was optimal for capturing the freezing level height development. Even for APR16, where there's no real agreement between simulated and real data, this lead time produces relatively small error values.

4.5. Ensemble performance

To understand the ensemble performance, we plot the observed hietograph and temperature series against the red region denoting the time at which more than 50% of the WRF ensemble predict rainfall (Figure 4.7). In the figure we also plotted the 25^{th} , 50^{th} and 75^{th} percentiles of the temperatures simulated by the ensemble.

The occurrence of the main pulses of the OCT15 event is very well predicted, although a final pulse that did not happen in October 20^{th} is produced. At the time of the rainfall peak the ensemble simulates a temperature $\sim 2°$C higher than the observed one, due to the abrupt temperature decrement prior to the rainfall beginning.

On the other hand, the WRF ensemble fails in identifying the temporal distribution of the more intense APR16 rainfall event with a 48 h delay in the prediction of the occurence (Figure 4.7, central plot). However, a thrid rainfall pulse predicted by the ensemble matches the

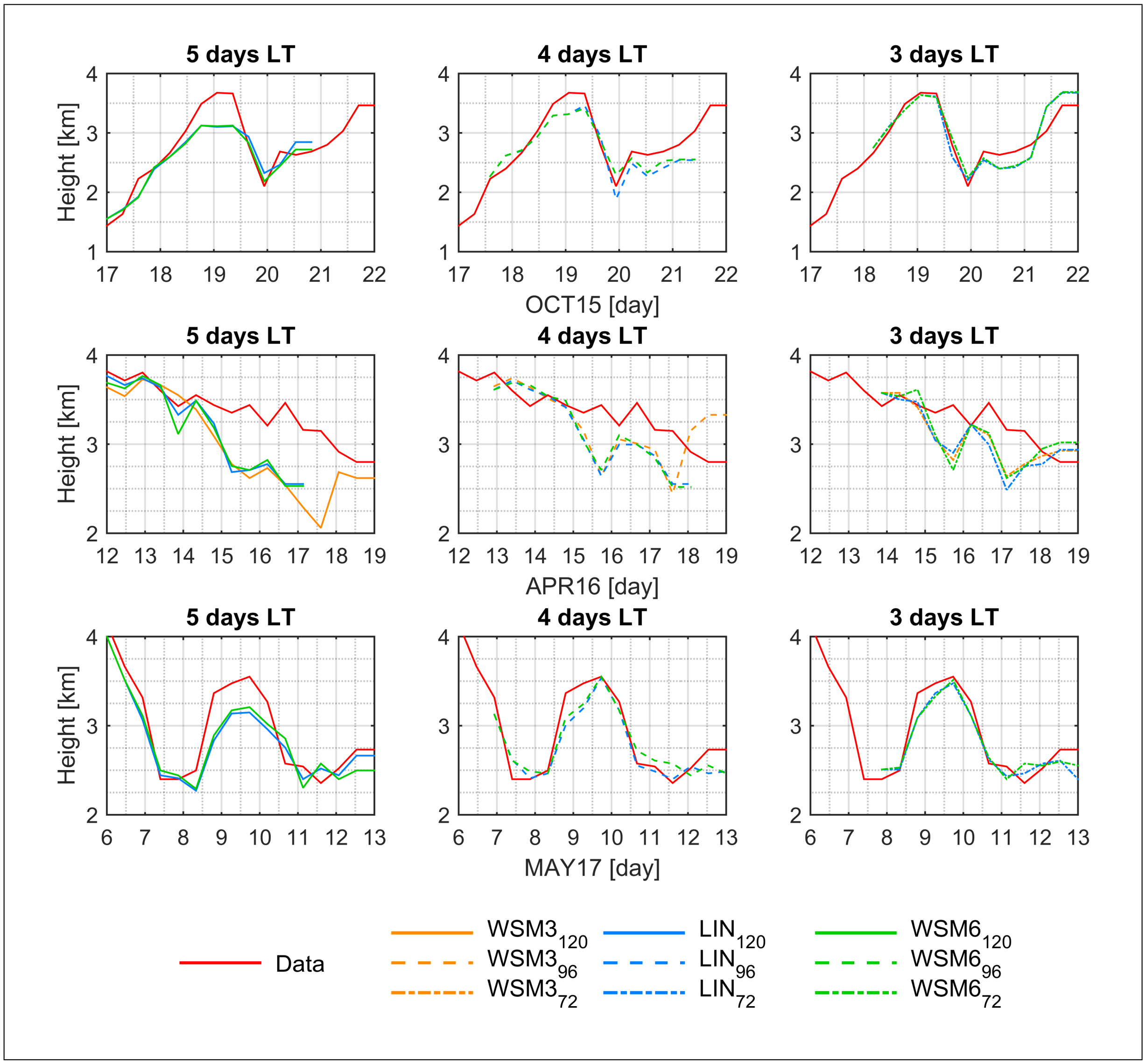

FIGURE 4.6. Freezing level height simulated with lead times (LT) of 5 (left), 4 (center) and 3 days (right), for OCT15 (upper row), APR16 (central row) and MAY17 (lower row) events

observed rainfall, which can lead to wrong conclusions. As mentioned in Garreaud (2013), the warm storms last from 12 to 36 h, coupled with an air temperature drop (>3°C) and the highest precipitation within the first hours of the event. These conditions indeed occurred during the APR16 event, particualrly the pulse starting on April 17^{th}. The ensemble underestimates the observed temperature for ~ 2 days before the rainfall initiates, but during its peak, this temperature was contained between the 25^{th} and 75^{th} percentiles.

The ensemble performance for the MAY17 event was more difficult to analyze, due to the frontal characteristics of the event. Although unable to exactly predict the observed rainfall occurence, the ensemble clearly simulates two different portions where precipitation happens. Rain is not properly predicted in the main period of intensive rainfall (11^{th} May), with only two of the three larger intensities being matched by discontinuous red stripes. Temperature is accurately predicted during the first rainfall event peak, but for the main peak there is a $\sim 2°$C overestimation.

Overall, the WRF ability to simulate frontal rainfalls is enhanced with a proper initial scheme parametrization, such as LIN or WSM6. In addition, the accurate prediction of rainfall is still too complicated over the complex topography of Santiago.

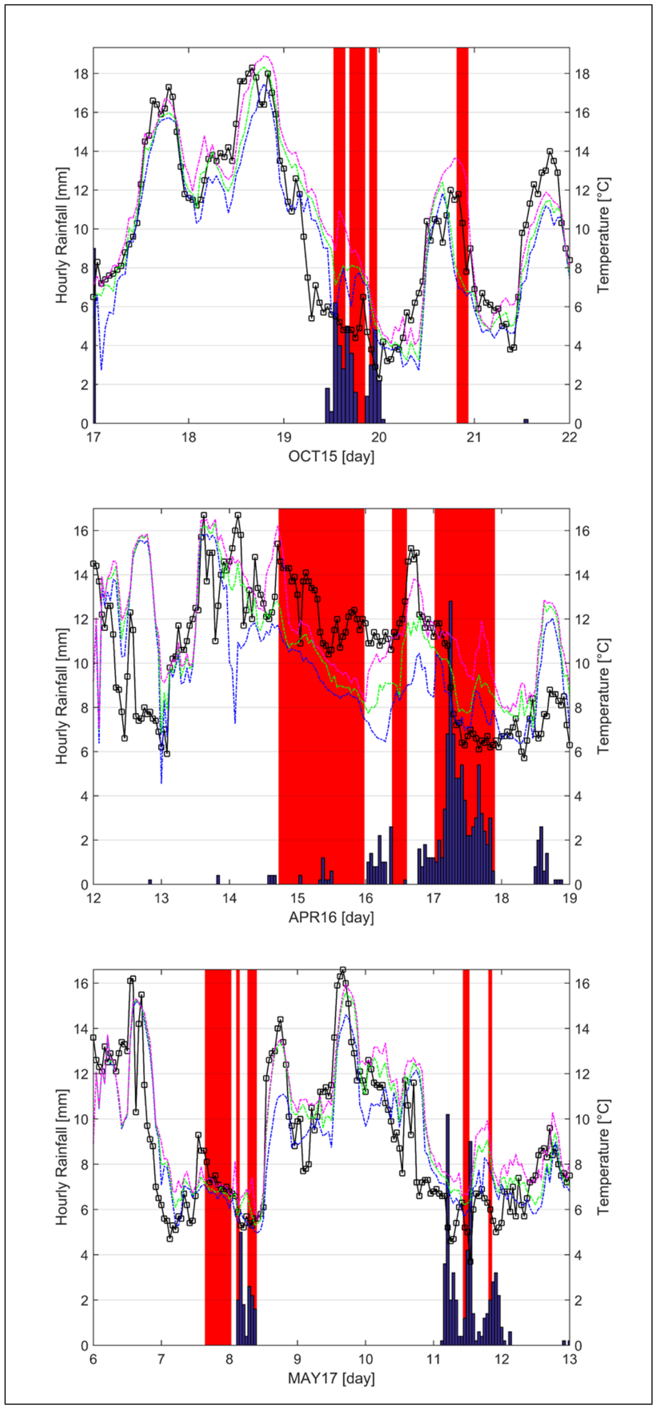

FIGURE 4.7. Ensemble performance for OCT15 (upper plot), APR16 (central plot) and MAY17 (lower plot) events. Red stripes indicate WRF rain occurrence prediction when the ensemble probability of rain exceeds 0.5. Temperature time series includes 25^{th} (blue), 50^{th} (green) and 75^{th} (magenta) percentiles for the ensemble forecast against observed data (black squares)

5. CONCLUSIONS AND FUTURE RESEARCH

Rainfall forecast over complex topography using WRF was studied through the simulation of three events between 2015 and 2017 in Quebrada de Ramón, a 38 Km^2 mountainous Andean watershed in central Chile. Several mycrophysics (MP) parametrizations (i.e. LIN, WSM6 and WSM3, currently used by the Chilean Weather Agency) were tested to find an optimum model performance. The simulations considered an horizontal resolution of 6 Km and 50 vertical levels for improving atmospheric temperature profiles, as well as $0.5°$ grid resolution GFS dataset. A realistic representation of Santiago's urban area was provided by MODIS, and Noah-MP model was used as land surface model. Finally, variable lead times of 72, 96 and 120 h before the rainfall start were also analyzed.

The unevenly prediction of rainfall length and total amount by the LIN and WSM6 parameterizations tends to improve with shorter lead times. For example, in the APR16 event, both schemes performed slightly better than WSM3 scheme with a 72 h lead time (with an IoA value of 0.66 and 0.62 respectively against the 0.59 value for the default configuration). Both performed better than WSM3, mainly for temperatures and rainfall intensities. In the OCT15 event, the positive trend related to lead time was not clear, but the mean value of the three lead times provide a IoA = 0.44 for WSM6 scheme and IoA = 0.40 for LIN. Finally, the MAY17 event was better captured via the LIN scheme (mean value IoA = 0.42). The WSM6 scheme has a lower IoA mean value (0.36) given the poor performance for the simulation with the shorter lead time, likely due to its meteorological characteristics.

The N-rainiest consecutive hours (NRH), a relevant characteristic of storm events given the impact on the hydrologic response, could not be well predicted by any of the MP options for cutoff low events. Negative biases were simulated in the OCT15 and MAY17 events, where the simulation with the larger lead time has the smaller bias. Differences among schemes are generally small (< 3 mm). Frontal system events were better captured (i.e. values spread contains the observed value), mostly via the WSM6 MP option, which also correctly predicted the concurrent temperatures with high intensities. Values of $T_{NRH(5)}$ MAE are smaller in the WSM6 option, although differences among schemes are small (~ 0.2°C). For example, in the APR16 event, the WSM6 option has a smaller bias than the WSM3 and

LIN option (2°C against 2.4°C and 2.5°C respectively).This is very relevant, as high flows and potential floods are typically produced by warm events when high temperatures and rainfall take place at the sime time (Garreaud, 2013).

The temporal evolution of precipitation, temperature and freezing level height were properly predicted for shorter lead times, especially for frontal system events, while complex meteorological cutoff low characteristics lead to poor forecasts. No clear trends in lead times were found, but shorter values (72 h ahead rainfall event) tended to provide more accurate simulations.

From our results, the WSM6 scheme resulted to be the best to simulate rainfall events in the Andean watershed under study. Nevertheless, rainfall simulation in WRF over complex topography is still a challenging issue, and its ability to accurately simulate rainfall, particularly non-frontal, events over Chilean central mountainous and foothills areas, where some of the main cities are located, is far from ideal. Further investigation should focus on simulating more rainfall events for which observed data could be available, as well as testing additional microphyisical schemes such as Thompson scheme (Thompson et al., 2008) or the Aerosol-aware Thompson scheme (Thompson & Eidhammer, 2014).

Finally, it would be of interest to improve rainfall forecast by combining a NWP tool with geostatistical methods, which take into account observed spatial attributes of the precipitation in the area. This geostatistical approach would eventually offset WRF forecasts problems over the Andean complex topography.

References

Aguilar, X. (2010). *Análisis de eventos extremos de precipitación en División Los Bronces, Cordillera central de Chile*. Tesis para optar al título profesional de meteorólogo, Departamento de Meteorología, Universidad de Valparaíso, Valparaíso.

Alfieri, L., Bisselink, B., Dottori, F., Naumann, G., Roo, A., Salamon, P., et al. (2016). Global projections of river flood risk in a warmer world. *Earth's Future*, *5*(2), 171-182.

Aligo, E. A., Gallus, W. A., & Segal, M. (2009). On the impact of WRF model vertical grid resolution on midwest summer rainfall forecasts. *Weather and Forecasting*, *24*(2), 575-594.

Arnold, D., Morton, D., Schicker, I., Seibert, P., Rotach, M. W., Horvarth, K., et al. (2012). Issues in high-resolution atmospheric modeling in complex topography - The HiRCoT workshop. *Croatian Meteorological Journal*, *47*(47), 3-11.

Bauer, P., Thorpe, A., & Brunet, G. (2015). The quiet revolution of numerical weather prediction. *Nature*, *525*, 4755.

Bongioannini Cerlini, P., Emanuel, K. A., & Todini, E. (2005). Orographic effects on convective precipitation and space-time rainfall variability: preliminary results. *Hydrology and Earth System Sciences*, *9*(4), 285–299.

Bozkurt, D., Rondanelli, R., Garreaud, R., & Arriagada, A. (2016). Impact of warmer eastern tropical pacific sst on the march 2015 atacama floods. *Monthly Weather Review*, *144*(11), 4441-4460.

Buizza, R., & Leutbecher, M. (2015). The forecast skill horizon. *Quarterly Journal of the Royal Meteorological Society*, *141*(693), 3366–3382.

Caneo, M. (2010). *Sensibilidad a diferentes esquemas de microfísica del WRF, en Chajnator-Chile*. Tesis para optar al título profesional de meteorólogo, Departamento de Meteorología, Universidad de Valparaíso, Valparaíso.

Carvalho, D., Rocha, A., Gomez-Gesteira, M., & Santos, C. (2012). A sensitivity study of the WRF model in wind simulation for an area of high wind energy. *Environmental Modelling & Software*, *33*, 23-34.

Catalán, M. (2013). *Acodicionamiento de un modelo hidrológico geomorfológico urbano de onda cinemática para su aplicación en cuencas naturales*. Tesis para optar al título profesional de ingeniero civil con diploma en ingeniería hidráulica, Departamento de Ingeniería Hidráulica y Ambiental, Pontificia Universidad Católica de Chile, Santiago.

Cheng, F.-Y., Hsu, Y.-C., Lin, P.-L., & Lin, T.-H. (2013). Investigation of the Effects of Different Land Use and Land Cover Patterns on Mesoscale Meteorological Simulations in the Taiwan Area. *Journal of Applied Meteorology and Climatology*, *52*(3), 570-587.

DGA. (2016). *Caracterización de suelos y generación de información meteorológica para prevención de riesgos hidrometeorológicos cuencas Salado y Copiapó* (Tech. Rep.). Dirección General de Aguas - Modelación Ambiental SPA.

Dimitrova, R., Silver, Z., Zsedrovits, T., Hocut, C. M., Leo, L. S., Sabatino, S. D., et al. (2016). Assessment of planetary boundary-layer schemes in the Weather Research and Forecasting mesoscale model using MATERHORN field data. *Boundary-Layer Meteorology*, *159*(3), 589-609.

Dirección General de Aeronáutica Civil (DGAC). (2018). *Dirección Meteorológica de Chile (DMC).*

Dudhia, J. (1989). Numerical study of convection observed during the winter monsoon experiment using a mesoscale two-dimensional model. *Journal of the Atmospheric Sciences*, *46*(20), 3077-3107.

Ek, M. B., Mitchell, K. E., Lin, Y., Rogers, E., Grunmann, P., Koren, V., et al. (2003). Implementation of noah land surface model advances in the national centers for environmental prediction operational mesoscale eta model. *Journal of Geophysical Research: Atmospheres*, *108*(D22).

Ekström, M. (2016). Metrics to identify meaningful downscaling skill in WRF simulations of intense rainfall events. *Environmental Modelling & Software*, *79*, 267-284.

EM-DAT. (2016). *The International Disaster Database* (Tech. Rep.). Centre for Research on the Epidemiology of Disasters (CRED), School of Public Health, Université Catolique de Louvain, Bélgica.

Evans, J. P., Ekström, M., & Ji, F. (2012). Evaluating the performance of a WRF physics ensemble over South-East Australia. *Climate Dynamics*, *39*(6), 1241-1258.

Fuenzalida, H., Sanchez, R., & Garreaud, R. (2005). A climatology of cutoff lows in the southern hemisphere. *Journal of Geophysical Research: Atmospheres*, *110*(D18).

Garreaud, R. (2013). Warm winter storms in central chile. *Journal of Hydrometeorology*, *14*(5), 1515-1534.

Garreaud, R., Falvey, M., & Montecinos, A. (2016). Orographic precipitation in coastal southern chile: mean distribution, temporal variability, and linear contribution. *Journal of Hydrometeorology*, *17*(4), 1185-1202.

Garreaud, R., & Fuenzalida, H. (2007). The influence of the andes on cutoff lows: A modeling study. *Monthly Weather Review*, *135*(4), 1596-1613.

Garreaud, R., & Rutllant, J. (1997). Precipitación estival en los andes de chile central: aspectos climatológicos. *Atmósfera*, *10*(1), 191-211.

Gneiting, T., & Raftery, A. E. (2005). Weather forecasting with ensemble methods. *Science*, *310*(5746), 248–249.

Goger, B., Rotach, M. W., Gohm, A., Stiperski, I., & Fuhrer, O. (2016, July). Current challenges for numerical weather prediction in complex terrain: Topography representation and parameterizations. In *2016 International Conference on High Performance Computing & Simulation (HPCS)* (p. 890-894).

Grell, G. A. (1993). Prognostic evaluation of assumptions used by cumulus parameterizations. *Monthly Weather Review*, *121*(3), 746-787.

Hirabayashi, S., Kroll, C. N., & Nowak, D. J. (2011). Component-based development and sensitivity analyses of an air pollutant dry deposition model. *Environmental Modelling & Software*, *26*(6), 804-816.

Hong, S.-Y., & Lim, J.-O. J. (2006). The WRF single-moment 6-class microphysics scheme (WSM6). *J. Korean Meteor. Soc.*, *42*(2), 129-151.

Houze, R. A. (2012). Orographic effects on precipitating clouds. *Reviews of Geophysics*, *50*(1).

Jiménez, P. A., & Dudhia, J. (2012). Improving the representation of resolved and unresolved topographic effects on surface wind in the WRF model. *Journal of Applied Meteorology and Climatology*, *51*(2), 300-316.

Jiménez, P. A., González-Rouco, J. F., García-Bustamante, E., Navarro, J., Montávez, J. P., Arellano, J. V.-G. de, et al. (2010). Surface wind regionalization over complex terrain: Evaluation and analysis of a high-resolution WRF simulation. *Journal of Applied Meteorology and Climatology*, *49*(2), 268-287.

Jiménez-Esteve, B., Udina, M., Soler, M., Pepin, N., & Miró, J. (2018). Land use and topography influence in a complex terrain area: A high resolution mesoscale modelling study over the Eastern Pyrenees using the WRF model. *Atmospheric Research*, *202*, 49 - 62.

Karki, R., Hasson, S. ul, Gerlitz, L., Schickhoff, U., Scholten, T., & Böhner, J. (2017). Quantifying the added value of convection-permitting climate simulations in complex terrain: a systematic evaluation of WRF over the Himalayas. *Earth System Dynamics*, *8*(3), 507-528.

Katragkou, E., García-Díez, M., Vautard, R., Sobolowski, S., Zanis, P., Alexandri, G., et al. (2015). Regional climate hindcast simulations within EURO-CORDEX: evaluation of a WRF multi-physics ensemble. *Geoscientific Model Development*, *8*(3), 603-618.

Kendall, M. G. (1975). *Rank Correlation Methods* (4th ed.). London: Griffin, Charles.

Kim, J.-H., Shin, D.-B., & Kummerow, C. (2013). Impacts of a priori databases using six WRF microphysics schemes on passive microwave rainfall retrievals. *Journal of Atmospheric and Oceanic Technology*, *30*(10), 2367-2381.

Kundzewicz, Z. W., Kanae, S., Seneviratne, S. I., Handmer, J., Nicholls, N., Peduzzi, P., et al. (2014). Flood risk and climate change: global and regional perspectives. *Hydrological Sciences Journal*, *59*(1), 1-28.

Lee, J. A., Kolczynski, W. C., McCandless, T. C., & Haupt, S. E. (2012). An objective methodology for configuring and down-selecting an NWP ensemble for low-level wind prediction. *Monthly Weather Review*, *140*(7), 2270-2286.

Lin, T., Farley, R. D., & Orville, H. D. (1983). Bulk parameterization of the snow field in a cloud model. *Journal of Climate and Applied Meteorology*, *22*(6), 1065-1092.

Lorente-Plazas, R., Jiménez, P. A., Dudhia, J., & Montávez, J. P. (2016). Evaluating and improving the impact of the atmospheric stability and orography on surface winds in the WRF mode. *Monthly Weather Review*, *144*(7), 2685-2693.

Madala, S., Satyanarayana, A. N. V., Srinivas, C. V., & Boadh, R. (2014, December). Sensitivity of PBL schemes of WRF-ARW model in simulating mesoscale atmospheric flow-field parameters over a complex terrain. In *Agu fall meeting abstracts* (p. A43A-3242).

Mann, H. B. (1945). Nonparametric tests against trend. *Econometrica*, *13*(3), 245–259.

Mass, C. F., Ovens, D., Westrick, K., & Colle, B. A. (2002). Does increasing horizontal resolution produce more skillful forecasts? *Bulletin of the American Meteorological Society*, *83*(3), 407-430.

Mlawer, E. J., Taubman, S. J., Brown, P., Iacono, M. J., & Clough, S. A. (1997). Radiative transfer for inhomogeneous atmospheres: RRTM, a validated correlated-k model for the longwave. *Journal of Geophysical Research: Atmospheres*, *102*(D14), 16663-16682.

MOP. (2013). *Manual de drenaje urbano: Guía para el diseño, construcción, operación y conservación de obras de drenaje urbano* (Tech. Rep.). Ministerio de Obras Públicas - Dirección General de Aguas.

Nakanishi, M., & Niino, H. (2006). An improved MellorYamada level-3 model: Its numerical stability and application to a regional prediction of advecting fog. *Boundary-Layer Meteorology*, *119*(2), 397-407.

Niu, G.-Y., Yang, Z.-L., Mitchell, K. E., Chen, F., Ek, M. B., Barlage, M., et al. (2011). The community Noah land surface model with multiparameterization options (Noah-MP): 1. Model description and evaluation with local-scale measurements. *Journal of Geophysical Research: Atmospheres*, *116*(D12), n/a-n/a.

Otarola, S., Dimitrova, R., Leo, L., Alcafuz, R., Escauriaza, C., Arroyo, R., et al. (2016). On the role of the Andes on weather patterns and related environmental hazards in Chile. In 19^{th} *joint conference on the applications of air pollution meteorology with the a&wma.*

Pontoppidan, M., Reuder, J., Mayer, S., & Kolstad, E. W. (2017). Downscaling an intense precipitation event in complex terrain: the importance of high grid resolution. *Tellus A: Dynamic Meteorology and Oceanography*, *69*(1), 1271561.

Puliafito, S., Allende, D., Mulena, C., Cremades, P., & Lakkis, S. (2015). Evaluation of the WRF model configuration for Zonda wind events in a complex terrain. *Atmospheric Research*, *166*, 24 - 32.

Rahn, D. A., & Garreaud, R. (2010). Marine boundary layer over the subtropical southeast Pacific during VOCALS-REx. Part 1: Mean structure and diurnal cycle. *Atmospheric Chemistry and Physics*, *10*(10), 4491-4506.

Roney, J. A. (2007). Statistical wind analysis for near-space applications. *Journal of Atmospheric and Solar-Terrestrial Physics*, *69*(13), 1485 - 1501.

Ruiz, J. J., Saulo, C., & Nogués-Paegle, J. (2010). WRF Model sensitivity to choice of parameterization over South America: Validation against surface variables. *Monthly Weather Review*, *138*(8), 3342-3355.

Saide, P. E., Carmichael, G. R., Spak, S. N., Gallardo, L., Osses, A. E., Mena-Carrasco, M. A., et al. (2011). Forecasting urban PM10 and PM2.5 pollution episodes in very stable nocturnal conditions and complex terrain using WRF-Chem CO tracer model. *Atmospheric Environment*, *45*(16), 2769-2780.

Seaman, N., Gaudet, B., Zielonka, J., & Stauffer, D. (2009). Sensitivity of vertical structure in the stable boundary layer to variations of the WRF models Mellor Yamada Janjic turbulence scheme. In *In* 9^{th} *wrf users workshop.*

Siddique, R., Mejia, A., Brown, J., Reed, S., & Ahnert, P. (2015). Verification of precipitation forecasts from two numerical weather prediction models in the middle Atlantic region of the USA: A precursory analysis to hydrologic forecasting. *Journal of Hydrology*, *529*(3), 1390-1406.

Sikder, S., & Hossain, F. (2016). Assessment of the weather research and forecasting model generalized parameterization schemes for advancement of precipitation forecasting in monsoon-driven river basins. *Journal of Advances in Modeling Earth Systems*, *8*(3), 12101228.

Siuta, D., West, G., & Stull, R. (2017). WRF hub-height wind forecast sensitivity to PBL scheme, grid length, and initial condition choice in complex terrain. *Weather and Forecasting*, *32*(2), 493-509.

Skamarock, W. C., Klemp, J. B., Dudhia, J., Gill, D. O., Barkerand, D. M., Duda, M. G., et al. (2008). *A description of the Advanced Research WRF Version 3* (NCAR technical note). Boulder CO: NCAR.

Soltanzadeh, I., Bonnardot, V., Sturman, A., Quénol, H., & Zawar-Reza, P. (2017). Assessment of the ARW-WRF model over complex terrain: the case of the Stellenbosch Wine of Origin district of South Africa. *Theoretical and Applied Climatology*, *129*, 1407-1427.

Thompson, G., & Eidhammer, T. (2014). A study of aerosol impacts on clouds and precipitation development in a large winter cyclone. *Journal of the Atmospheric Sciences*, *71*(10), 3636-3658.

Thompson, G., Field, P. R., Rasmussen, R. M., & Hall, W. D. (2008). Explicit forecasts of winter precipitation using an improved bulk microphysics scheme. part ii: Implementation of a new snow parameterization. *Monthly Weather Review*, *136*(12), 5095-5115.

Vargas, X. (1999). Corrientes de detritos en la Quebrada de Macul, Chile. Estudio de caudales máximos. *Ingeniería del Agua*, *6*(4), 341-344.

Wilcox, A. C., Escauriaza, C., Agredano, R., Mignot, E., Zuazo, V., Otárola, S., et al. (2016). An integrated analysis of the March 2015 Atacama floods. *Geophysical Research Letters*, *43*(15), 8035-8043.

Willmott, C. J., Robeson, S. M., & Matsuura, K. (2012). A refined index of model performance. *International Journal of Climatology*, *32*(13), 2088-2094.

Zegpi, M., & Fernández, B. (2010). Hydrological model for urban catchments analytical development using copulas and numerical solution. *Hydrological Sciences Journal*, *55*(7), 1123 - 1136.

Zhang, H., & Pu, Z. (2010). Beating the uncertainties: Ensemble forecasting and ensemble-based data assimilation in modern numerical weather prediction. *Advances in Meteorology*, *2010*, 10.

Zhang, H., Pu, Z., & Zhang, X. (2013). Examination of errors in near-surface temperature and wind from WRF numerical simulations in regions of complex terrain. *Weather and Forecasting*, *28*(3), 893-914.

APPENDICES

APPENDIX A. ABBREVIATIONS

Here are included some recurrent abbreviations used in this document, to facilitate the reading of this thesis.

TABLE A.1. Abbreviations used in this study

Abbreviation	Meaning
APR16	17^{th} April 2016 rainfall event
ARW	Advanced Research WRF
DGAC	Directorate General of Civil Aviation
	(Dirección General de Aeronáutica Civil)
DMC	Chilean Weather Agency
	(Dirección Meteorológica de Chile)
FNL	NCEP Final Operational Global Analysis data
GCM	Global Circulation Model
GFS	Global Forecast System data
IEAT	Inter-event arrival time
IoA	Index of Agreement
LIN	Lin et al. MP scheme
LSM	Land Surface Model
LU	Land Use
MAE	Mean absolute error
MAY17	11^{th} May 2017 rainfall event
MODIS	Moderate Resolution Imaging Spectroradiometer
MP	Microphysics
MYNN	Mellor-Yamada Nakanishi Niino PBL scheme
NAM	North American Mesoscale Forecast System
NCAR	National Center for Atmospheric Research
NCEP	National Center for Environmental Prediction
Noah	Acronym of: (1) NCEP, (2) Oregon State University

continued ...

Table A.1 continued from previous page

Abbreviation	Meaning
	(3) Air Force and (4) Hydrology Lab NWS
Noah-MP	Noah - Multiparametrization model
NRH	N-rainiest consecutive hours
NSE	Nash-Sutcliffe Efficency coefficient
NWP	Numerical Weather Predictor
OCT15	19^{th} October 2015 rainfall event
PBL	Planet Boundary Layer
RRTM	Rapid Radiative Transfer Model
RUC	Rapid Update Cycle
SL	Surface Layer
SST	Sea surface temperature
T_{NRH}	Temperatures time series associated with each NRH
USGS	United States Geological Survey
WRF	Weather Research and Forecast
WSM3	WRF-Single-Moment-Microphysics 3-Class MP scheme
WSM6	WRF-Single-Moment-Microphysics 6-Class MP scheme

APPENDIX B. WRF MODEL

WRF is a physically-based model, via a set of equations that follows the mass coordinates. This equations, in terms of a terrain-following hydrostatic pressure vertical coordinate η, allow us to represent the terrain topographic characteristics more accuratelly. The η coordinates (see equation B.1) are a lineal interpolation between the surface and top boundaries pressures (p_{hs} and p_{ht}, respectively), according to the hydrostatic component of pressure (p_h):

$$\eta = \frac{p_h - p_{ht}}{\mu} \qquad \mu = p_{hs} - p_{ht} \tag{B.1}$$

In this formulation, $\mu\,(x, y)$ represents the mass per unit area within the column in a (x, y) location inside the domain: this transforms the flux variables to become $\mathbf{V} = \mu\mathbf{v} = (U, V, W)$, $\Theta = \mu\theta$ and $Q_m = \mu q_m$. Here $\mathbf{v}$ represents the wind vector, q_m represents the mixing ratios for water phases (as vapor, cloud, rain, ice, snow, grapuel), θ is the temperature and α is the inverse density of the full parcel. The Euler equations of motion, as can be seen below, takes the preassure as independent variable:

$$\partial_t U + (\nabla \cdot \mathbf{V}u)_\eta + \mu\alpha\partial_x p + \partial_\eta p \partial_x \phi = F_U \tag{B.2}$$

$$\partial_t V + (\nabla \cdot \mathbf{V}v)_\eta + \mu\alpha\partial_y p + \partial_\eta p \partial_y \phi = F_V \tag{B.3}$$

$$\partial_t W + (\nabla \cdot \mathbf{V}w)_\eta - g\,(\partial_\eta p - \mu) = F_W \tag{B.4}$$

$$\partial_t \phi + (\mathbf{v} \cdot \nabla\phi)_\eta = gw \tag{B.5}$$

$$\partial_t \Theta + (\nabla \cdot \mathbf{V}\theta)_\eta = F_\Theta \tag{B.6}$$

$$\partial_t \mu + (\nabla \cdot \mathbf{V})_\eta = 0 \tag{B.7}$$

$$\partial_t Q_m + (\nabla \cdot \mathbf{V}q_m) = F_{Q_m} \tag{B.8}$$

$$\partial_\eta \phi = -\alpha\mu \tag{B.9}$$

$$p = p_0 \left(\frac{R\Theta}{p_0\alpha\mu}\right)^\gamma \tag{B.10}$$

The advantage of this coordinate system is to eliminate preassure using the gas law, just as in a height coordinate system: this way we avoid to integrate a non-conservative pressure equation. Prognostic equations B.2 to B.2 represents the momentum conservation in the x, y and z axis, respectively. In this set of equivalences, ϕ is the geopotential height, i.e., $\phi = gz$, with g being the aceleration due to gravity and z being the height coordinate. The geopotential (equation B.5) is also conserved over time and space (following η coordinates), in relation to the vertical wind aceleration. Equation B.6 represent the heat conservation, equation B.7 the mass conservation, and the equation B.8 represents the water conservation.

Finally, both diagnostic relations over hydrostatic pressure equation (equation B.9) and the gas law (equation B.10) are also included. For this last expresion, R represent the gas constant, $\gamma = \frac{C_p}{C_v} = 1.4$ is the ratio of the heat capacities for dry air, and $p_0 = 1000$ hPa.

WRF uses a 3^{rd} order Runge Kutta time integration to discretrize and solve this set of equations, although advection terms are in the form of a flux divergence. WRF cannot resolve all the physical processes with this set of equations, therefore physics schemes are used. These schemes quantify the contribution of numerically non-solved atmospheric processes in terms of variables already solved within the domain discrete grid. The schemes parameterizes the physical phenomena related to water phases in the atmosphere (MP and Cumulus), radiation (shortwave and longwave radiation) and the interaction between atmosphere and soil (PBL, Surface Layer and Land Surface), among others. The broad spectrum of parameterizations for each one of these schemes, developed to achieve a specific atmospheric characteristic, gives WRF the possibility to approach the same meteorological event from different physical formulations. Thus, different results can be obtained based on every one of these parameterizations, and the propper choice of them is also an important part of a meteorological simulation.

A diagram of how the WRF model works can be seen in Figure B.1. As input WRF needs gridded data, which can obtained from GCM in spatial resolutions from $1°$ to $0.25°$: among them GFS data is commonly used, but other meteorological forcings as RUC (Rapid Update Cycle), NAM (North American Mesoscale Forecast System) are also used, given the specific conditions and goals of every simulation. In general, these meteorological forcings contains a huge dataset of meteorological variables in a temporal resolution (hourly, 3 h, 6 h). The complete dataset for GFS input data can be found in http://rda.ucar.edu/datasets/ds084.1/, which contains different temperatures, albedo, snow variables, wind properties at different heights, geopotential height, land use classification, precipitation rate and amount, among others. WRF terrestrial data describes the regional and local topography properties, because the atmospere/soil interaction has a great importante in the flux exchange rates. WRF can also be run or improved with local observational data.

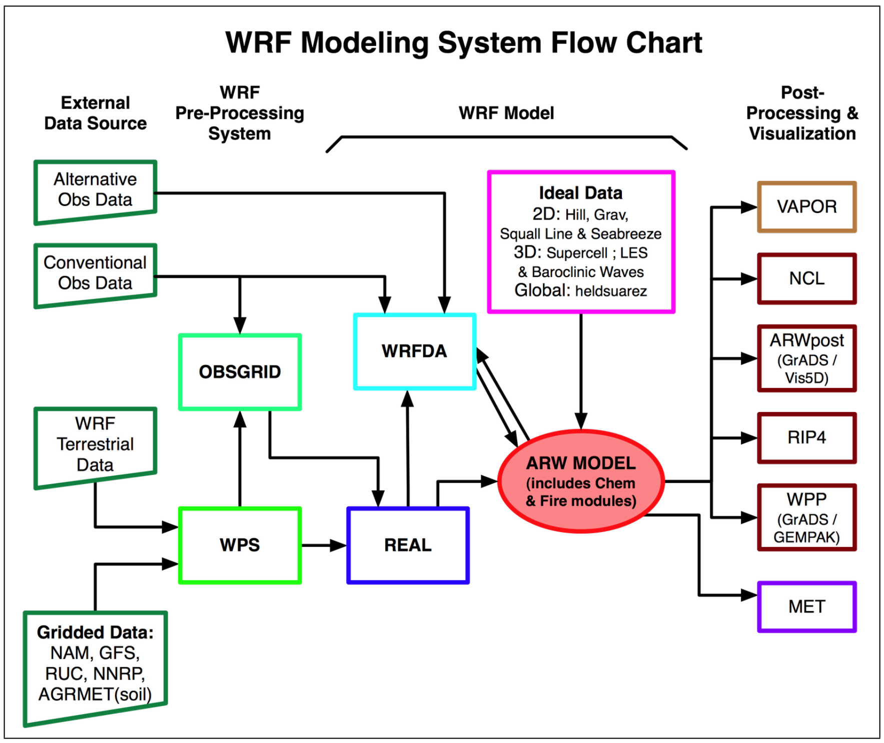

FIGURE B.1. WRF modeling system flow chart. From WRF User Manual, NCAR

The ARW-WRF model solves the atmospheric equations depicted above, in addition to the physical schemes selected, to transform and forecast the meteorological forcings in the domain resolution scale, with consideration of topography, land cover, land use and local characteristics. In this way, the WRF model takes the meteorological forcing in a coarse resolution and transform them, via prognostic and diagnostic equations, into local weather patterns that result from the complex local interactions between atmosphere, soil and ocean. Finally, WRF post-processing offers several options to manage data and visualize data, although any computing language or software can manage the output WRF files, in the netCDF format.

APPENDIX C. WRF WIND DIRECTION AND SPEED

Wind direction is defined according to the horizont point from which it comes, in sexagesimal degrees: $0°$ for North, $90°$ for East, $180°$ for South and $270°$ for West. Wind zonal (*u*) and meridional (*v*) components are provided directly by WRF (uvmet10), rotated to earth coordinates at 10 meters height. The wind magnitude (*ff*) is obtained by Eq. C.1:

$$ff = \sqrt{u^2 + v^2} \tag{C.1}$$

Wind direction (ϑ) is obtained by trigonometric relations, reminding differences between meteorological and euclidean degrees orientation. In order to invert the arctangent degree rotation, starting from North, Eq. C.2 must be used, where input variables are transformed from radians to sexagesimal degrees:

$$\vartheta = \begin{cases} \arctan\left(\frac{u}{v}\right) * \frac{180°}{\pi} & \text{if } (u,v) \geq 0 \\ \arctan\left(\left(\frac{u}{v}\right) + 2\pi\right) * \frac{180°}{\pi} & \text{if } u < 0, v > 0 \\ \arctan\left(\left(\frac{u}{v}\right) + \pi\right) * \frac{180°}{\pi} & \text{if } v < 0 \\ 90° & \text{if } v = 0, u > 0 \\ 270° & \text{if } v = 0, u < 0 \end{cases} \tag{C.2}$$

APPENDIX D. NASA SATELLITE IMAGES

To capture previous synoptic meteorological conditions, NASA EOSDIS worldview satellite images were analyzed (https://worldview.earthdata.nasa.gov/). For the three simulated rainfall events, satellite images are shown in Figures D.1, D.2, D.3. As can be seen, low pressure pattern is always present in front of the Chilean coastline.

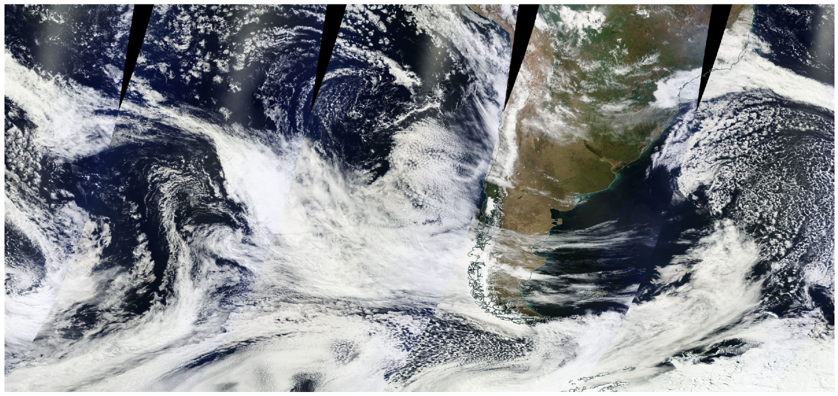

(A) 18^{th} October 2015

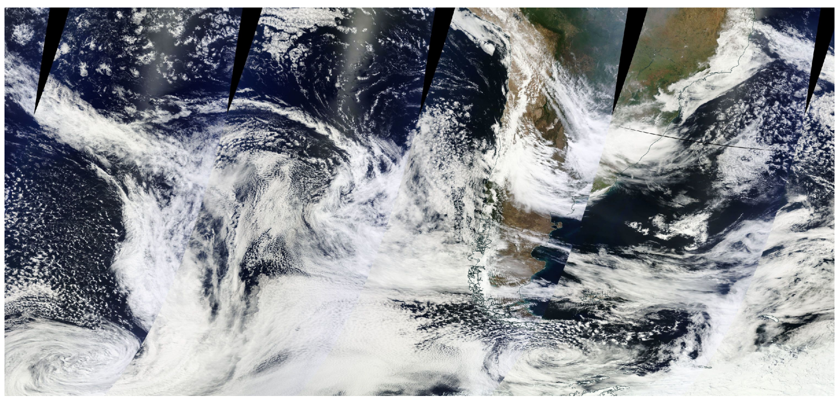

(B) 19^{th} October 2015

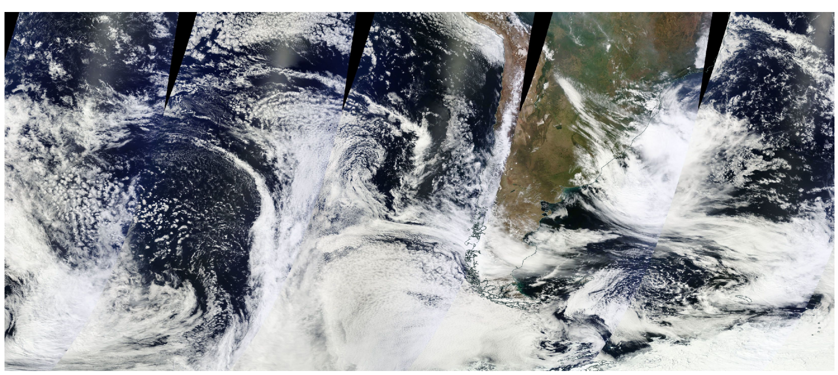

(C) 20^{th} October 2015

FIGURE D.1. NASA EOSDIS worldview satellite image for Santiago, 18^{th} -20^{th} October 2015

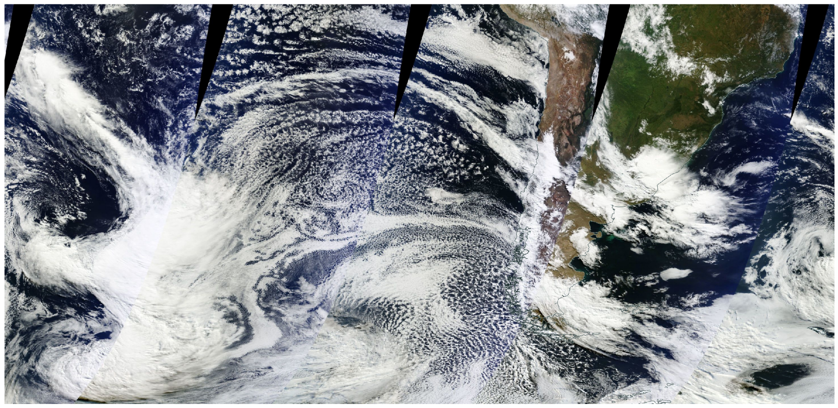

(A) 15^{th} April 2016

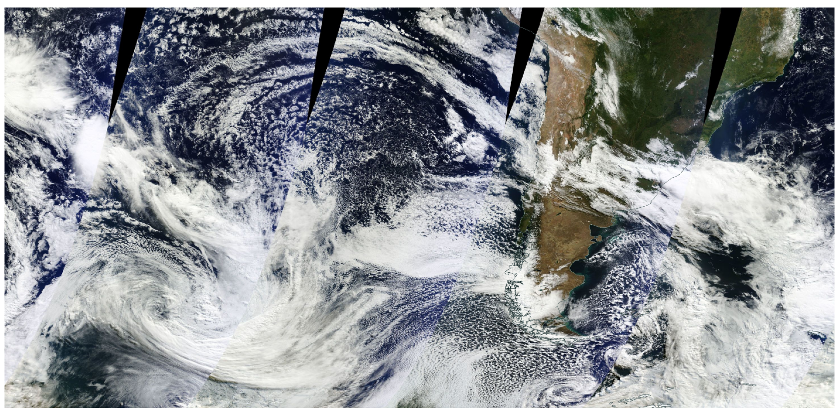

(B) 16^{th} April 2016

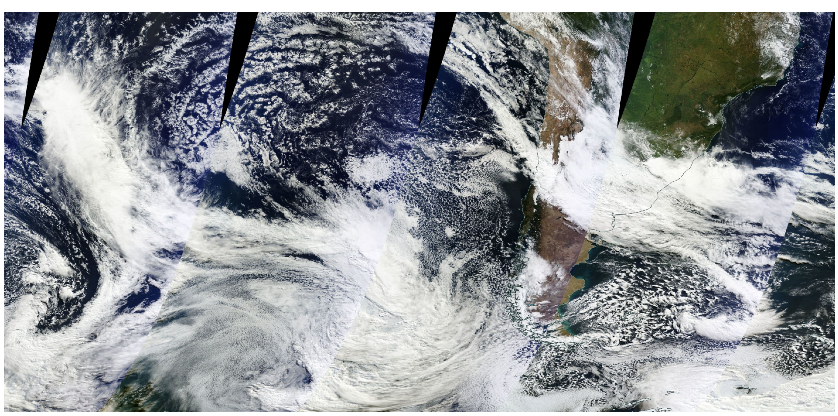

(C) 17^{th} April 2016

FIGURE D.2. NASA EOSDIS worldview satellite image for Santiago, 15^{th} - 17^{th} April 2016

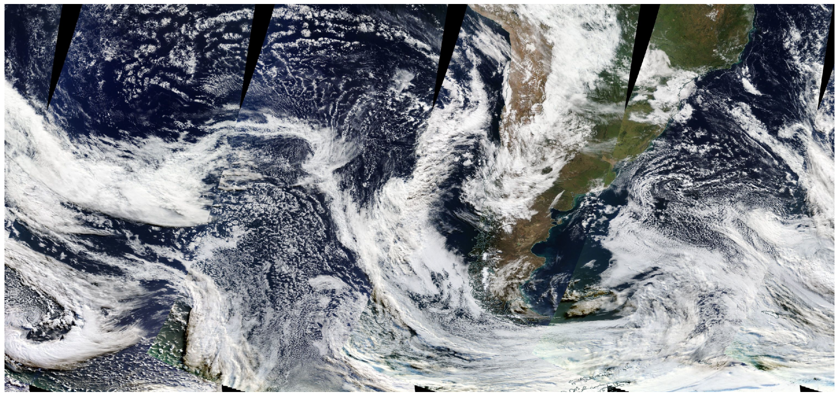

(A) 10^{th} May 2017

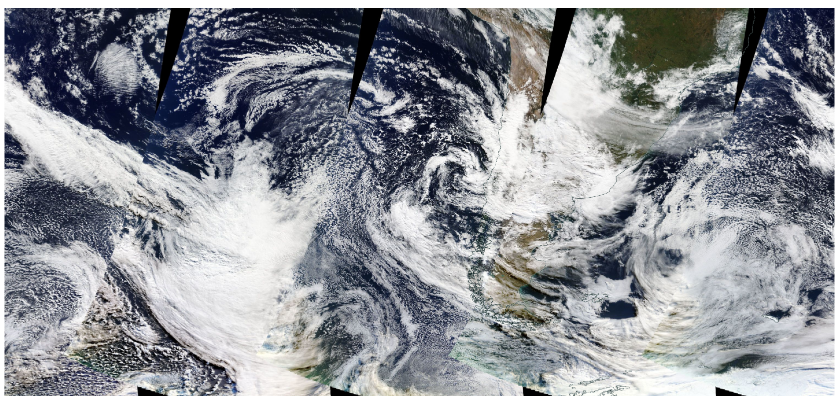

(B) 11^{th} May 2017

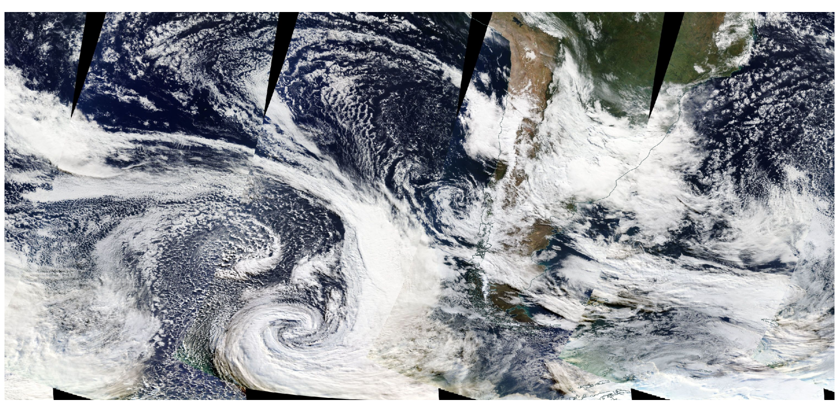

(C) 12^{th} May 2017

FIGURE D.3. NASA EOSDIS worldview satellite image for Santiago, 10^{th} - 12^{th} May 2017

APPENDIX E. QUEBRADA DE RAMÓN BASIN CHARACTERISTICS

To assess the similarity of watersheds we analyzed the hypsometric curve of Quebrada de Ramón basin, which provides information about basin height values and distribution. A non-dimensional hypsometric curve was used, based on the accumulated percentage of the basin area above every height (Figure E.1). The basin height data was obtained from a 90 m resolution DEM (Digital Elevation Model). The same coordinates dataset was used to obtain the hypsometric curve based on WRF model height, which is restrained only to 4 grids over the area.

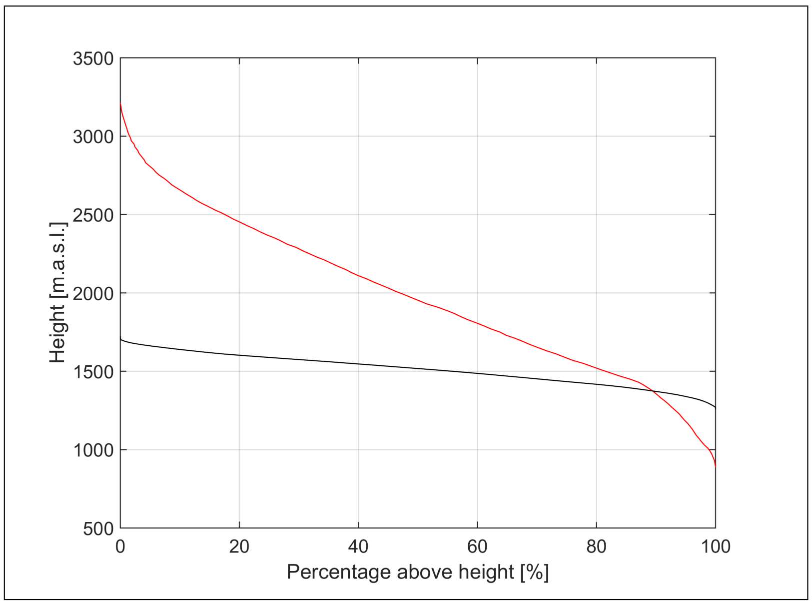

FIGURE E.1. Quebrada de Ramón's hypsometric curve, based on a 90 m resolution DEM. Basin hypsometric curve based on DEM (red line) and WRF curve based on grid height data (black line)

As can be seen, WRF undestimates the true basin topography since its height range is only between $1270 - 1700$ m.a.s.l., far away from real values of $900 - 3200$ m.a.s.l.. Thus, it doesn't reproduce the steep distribution of extreme values. This bad performance is inherent to the NWP constrains over topography, even more with a relativelly low resolution (~ 6 Km) for a small watershed such as Quebrada de Ramón.

APPENDIX F. VERTICAL LEVELS

Vertical levels discretization used for simulations differ not only in total number, but also in grid density. Both options have more densified grids near surface, where the η levels follows the topography corresponding to the simulation domain. In a range from 0 to 1, Figure F.1 shows this discretization, where 1.000 correspond to a η level in the surface level pressure (i.e., p_{hs} equal to 1000 hPa), and 0.000 is for a η level in the WRF model top height (i.e., p_{ht} equal to 50 hPa). The η level are calculated following the equation B.1, in Appendix B.

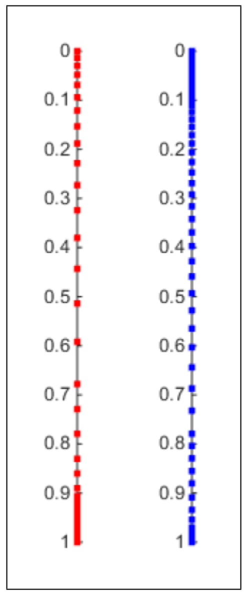

FIGURE F.1. WRF model vertical grid discretization, normalized by a factor of 1000 hPa, between 0 and 1. Red dots (left) correspond to 39 vertical levels (Saide et al., 2011) and blue (right) stands for WRF 50 vertical levels. The η-levels are more densified near to boundaries.

A detailed vertical density for both options is shown in Table F.1.

TABLE F.1. 39 & 50 vertical levels grid comparison

Vertical level	39 **vertical levels**	50 **vertical levels**
1	0	0
2	0.014	0.004
3	0.03	0.009

Continued on next page

Table F.1 – continued from previous page

Vertical level	39 vertical levels	50 vertical levels
4	0.048	0.014
5	0.069	0.02
6	0.094	0.026
7	0.121	0.033
8	0.153	0.04
9	0.188	0.048
10	0.228	0.056
11	0.273	0.065
12	0.324	0.075
13	0.38	0.086
14	0.443	0.098
15	0.514	0.11
16	0.592	0.124
17	0.678	0.139
18	0.729	0.154
19	0.779	0.171
20	0.83	0.188
21	0.86	0.206
22	0.89	0.226
23	0.906	0.247
24	0.917	0.269
25	0.924	0.292
26	0.932	0.316
27	0.938	0.342
28	0.945	0.369
29	0.953	0.397
30	0.961	0.428

Continued on next page

Table F.1 – continued from previous page

Vertical level	39 **vertical levels**	50 **vertical levels**
31	0.97	0.459
32	0.978	0.493
33	0.985	0.528
34	0.992	0.565
35	0.994	0.603
36	0.996	0.644
37	0.998	0.687
38	0.999	0.732
39	1	0.779
40		0.804
41		0.829
42		0.855
43		0.88
44		0.909
45		0.934
46		0.954
47		0.97
48		0.983
49		0.993
50		1

APPENDIX G. WRF PRELIMINARY MODIFICATIONS

G.1. Vertical levels test

A first stage of vertical levels density comparison was qualitatively made via Skew-T diagrams, focused in near surface level variables, such as temperature and wind speed and direction. A second quantitative comparison stage was made using statistics showed in section 3.4. The simulation goal was to elucidate the vertical density influence over simulations, so the remaining physic options were kept as DMC initial configuration (Table G.1).

TABLE G.1. Scheme configuration for vertical levels comparison

Physical scheme	Parametrization
Short-wave radiation	Dudhia
Long-wave radiation	RRTM
Cumulus	Grell 3D Ensemble
Planet Boundary Layer	MMYN 2.5
Soil Layer	MMYN
Land Surface Model	5-Layer Thermal Diffusion Scheme
Microphysics	WRF Single-moment 3-class

Skill scores were not very helpful to measure the influence of the vertical grid density, since they consider every simulated step as a whole, not like independent simulations of atmospheric conditions. As using time series as an indicator of the model performance may not be appropriate, a more detailed comparison is needed to perceive the simulated atmosphere development. In Table G.2 statistics of the vertical level test are shown.

Goodness of fit between simulated and observed data are far away from the desired values, with similar behaviour between them (Figure G.1). For all the meteorological variables, 50 vertical levels provided a slightly better performance, except in the temperature, which is underestimated before the storm peak, and overestimated after it.

TABLE G.2. Vertical levels test statistics

Statistic	Temperature		Wind speed		Wind direction	
	39	**50**	**39**	**50**	**39**	**50**
MAE	3.09	3.70	2.63	2.03	79.54	75.12
NSE	−0.72	−1.39	−35.05	−23.11	0.24	0.31
IoA	0.38	0.25	−0.67	−0.58	0.60	0.62

A final analysis of atmospheric stability was made via Skew-T diagrams, a very useful tool to scan the atmosphere status, presenting temperature and dew temperature vertical profiles, and also wind speed and direction vertical profiles. From this information, is possible to obtain vertical data for different temperatures (potential, equivalent, wet bulb, etc.), vapor pressures and mixing ratios. Also gives different height values at which some important microphysical phenomena happen (zero isotherm, lifting condensation level, convective condensation level, equilibrium level, among others). From the Skew-T diagram, a freezing level height similar for both simulations can be seen (Figure G.2), but it shows evident differences between dew temperature, temperature, wind speed and direction for 14^{th} April 2016 (12Z).

Slight differences in lower levels for temperature profiles allow that 50 vertical levels better reproduce a saturated atmosphere near surface, i.e. the presence of precipitation. In middle heights, 50 vertical levels captures better a dry section near to 6 Km height, with no further discrepancies with 39 vertical levels in upper levels.

Although none of them can't properly predict wind direction in these levels, the wind speed is almost well represented. In lower levels, the North / Northwest wind shows a warm advection, typical to the weather front beginning (3 days before the rainfall peak). For this reasons, and as a consequence of a more densified grid, 50 vertical levels were chosen for the final simulations.

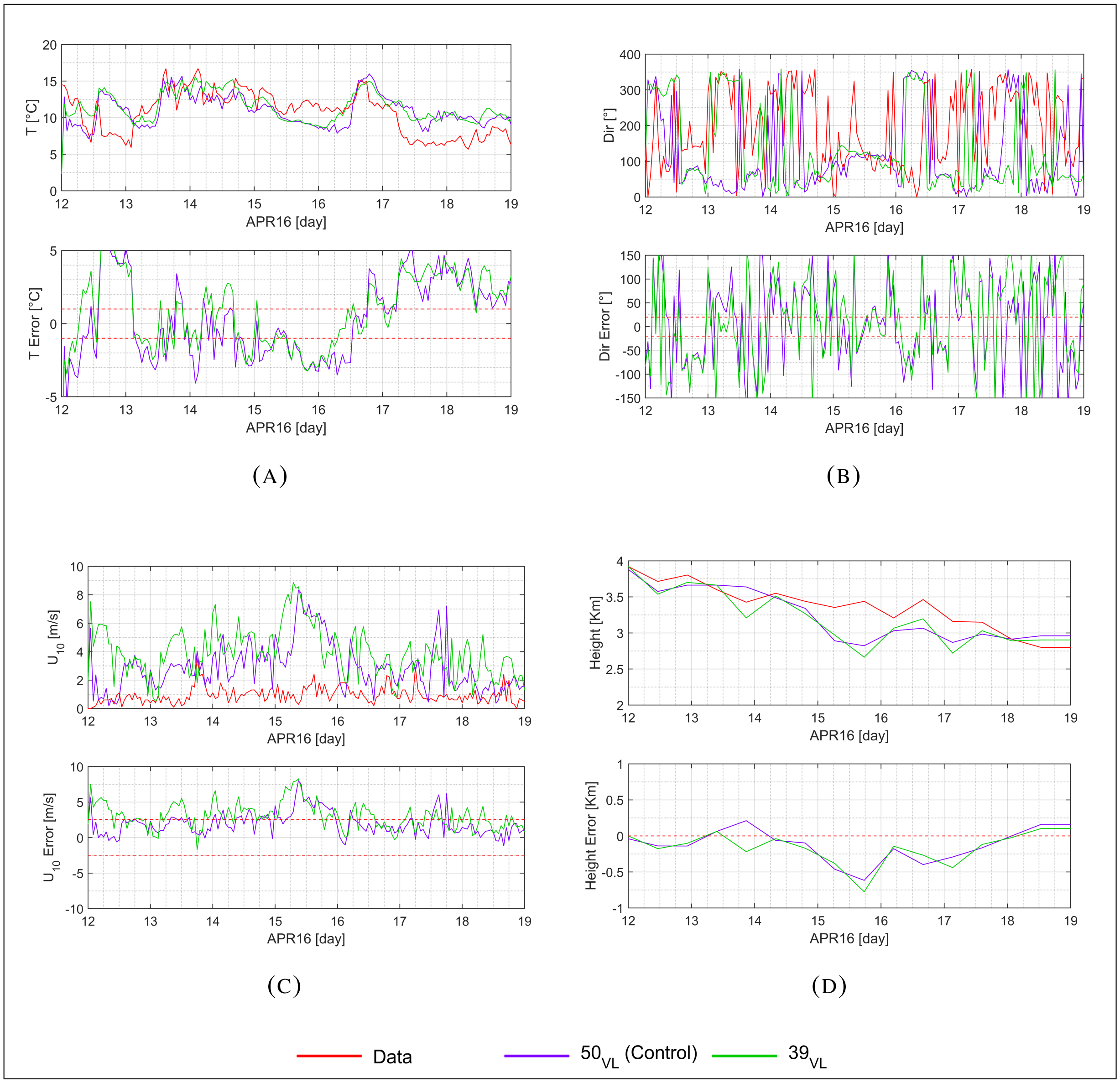

FIGURE G.1. Time series and error for vertical level test: (A) temperature, (B) wind direction, (C) wind speed and (D) freezing level height. In each subfigure the upper plot correspond to time series against observed data, and the lower plot is the error in every simulation step: red dashed line in (A)-(C) is the tolerance criterion (Table 3.2) and ideal error (D).

G.2. Land use and Land Surface Model

APR16 rainfall event was simulated to test LS and LSM by four different configurations (Table G.3). We emphasize error analysis near surface levels in temperature and wind speed and direction, and also the rainfall skill scores.

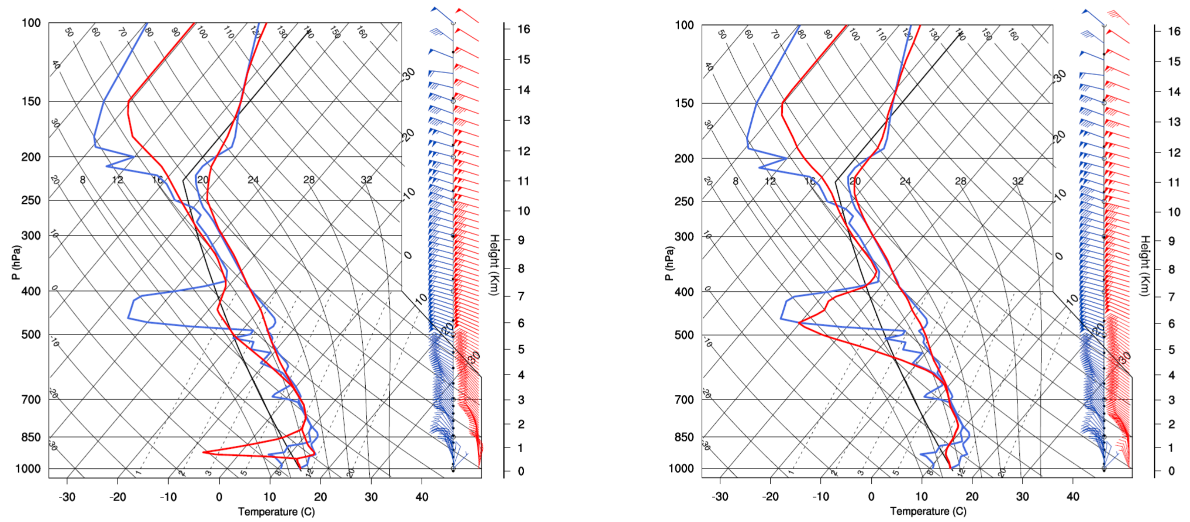

(A) 39 vertical levels

(B) 50 vertical levels

FIGURE G.2. Skew-T plots for vertical level test, 14^{th} April 2016 12Z. Vertical profiles represent dew temperature (left) and temperature (right), and wind speed and direction are represented via wind barbs. Observational data is in blue and WRF simulations are in red.

TABLE G.3. LU and LSM scheme configuration ensemble

Simulation	LU	LSM
S1	USGS	5 - Layer
S2	USGS	Noah
S3	MODIS	Noah
S4	MODIS	Noah- MP

Statistics for all the simulations present negligible differences and it is not easy to prove which one is the best, moreover when the time series have similar behaviour (Figure G.3). Once more, temperature time series is underestimated before the storm peak, and overestimated after it, but it is almost correct in the peak. MODIS LS provide a slightly higher score in temperature prediction, i.e. values inside the DMC tolerance. For wind speed, S4 simulation performs as the best of the group, but for wind direction there is no clear best option (Table G.4).

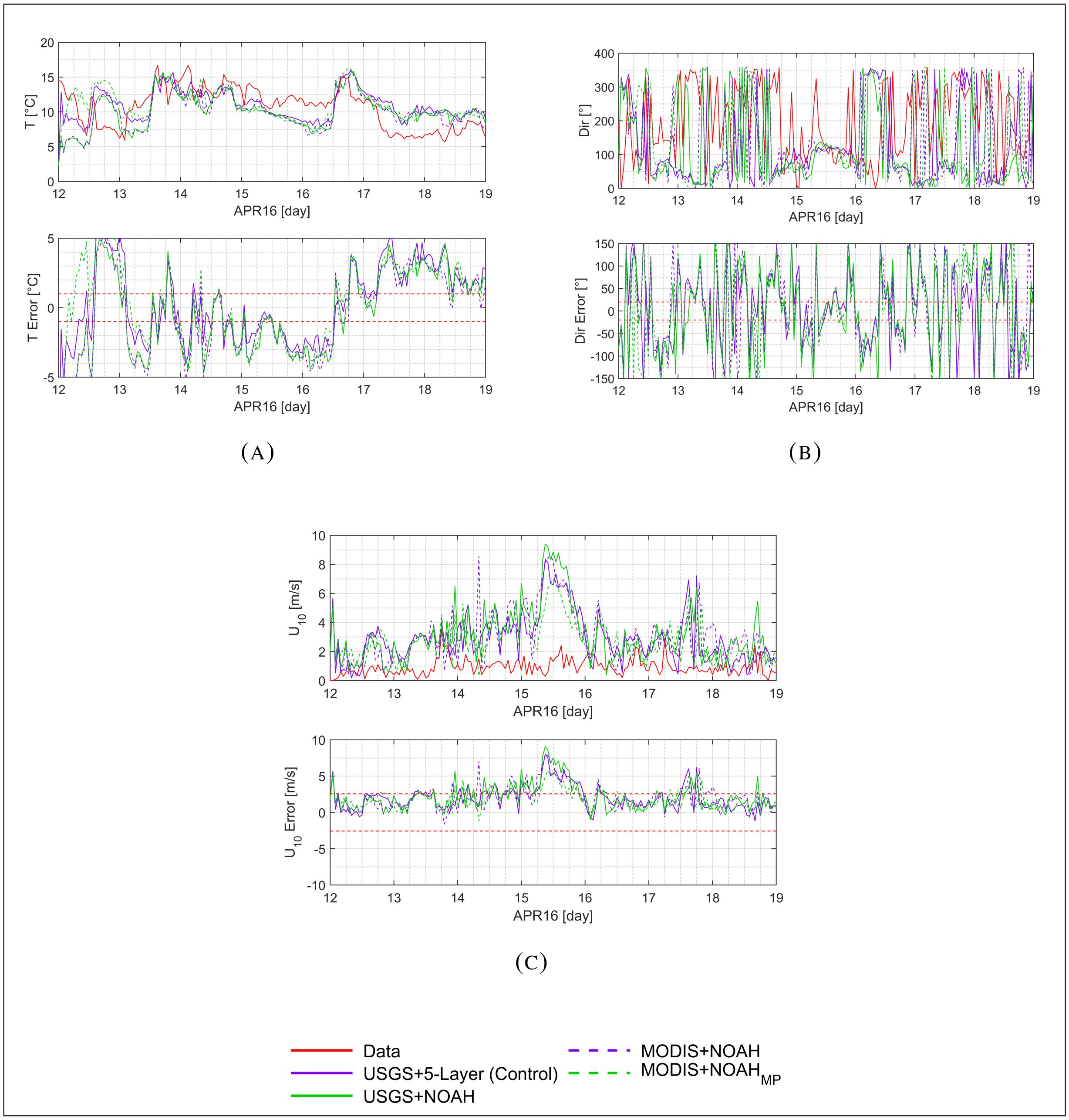

FIGURE G.3. Time series and error for LS and LSM test: (A) temperature, (B) wind direction and (C) wind speed. In every subfigure the upper plot correspond to time series against observational data (red line), and the lower plot is the error in every simulation time step (red dashed line is the tolerance criterion (Table 3.2)).

No decision was made based on statistics skills, due to the minimal differences between values. The decision to use MODIS was made based on Saide et al. (2011) conclusions over land use options. For LSM, Noah-MP was chosen for its best performance with the MODIS, but also for its better treatment of surface fluxes, which can capture temperature and wind variations near surface (Niu et al., 2011).

TABLE G.4. LS/LSM test statistics

Statistic	Temperature				Wind speed				Wind direction			
	S1	**S2**	**S3**	**S4**	**S1**	**S2**	**S3**	**S4**	**S1**	**S2**	**S3**	**S4**
MAE	2.42	2.66	2.67	2.5	2.07	2.22	2.17	1.89	75.1	77.5	75.0	79.9
NSE	0	−0.3	−0.3	−0.1	−20	−24	−22	−14	0.31	0.26	0.31	0.25
IoA	0.51	0.46	0.46	0.49	−0.6	−0.6	−0.6	−0.5	0.62	0.61	0.62	0.59

G.3. Initial and boundary condition data

APR16 simulation was made with GFS and FNL input dataset, just to get a notion of the improvement made with reanalysis data (FNL). In this case, we emphasized the skill score of simulated time series near surface (such as temperature, wind speed and direction), the rainfall temporal characteristics and freezing level height. Parametrizations chosen for simulations are shown in Table G.5.

TABLE G.5. GFS/FNL simulations configuration

Physical scheme	Parametrization
Short-wave radiation	Dudhia
Long-wave radiation	RRTM
Cumulus	Grell 3D Ensemble
Planet Boundary Layer	MMYN 2.5
Soil Layer	MMYN
Land Surface Model	Noah-MP
Microphysics	WRF Single-moment 3-class

Also the lead time variability was taken into account in this analysis, with a temporal range of 72 to 120 hours (3 - 5 days) before the rainfall peak day. As can be seen in Table G.6, GFS and FNL input data conveys to small differences. These are smaller for temperature as the lead time diminishes, providing FNL the best value for all the tested simulations. In fact, GFS_{120} has a constant underestimation of this time series, getting a smaller error with shorter lead times. In FNL simulations, the reanalysis improve this issue. Wind speed is similar predicted by both datasets, where none of them can accurately predict this variable, getting a worse score with shorter lead times. Wind direction exhibit good performance scores for both input data, with no clear best option. For rainfall, GFS data performed better, but simulated time series are far away from desirable values (NSE values primarily). (Complete time series can be found in Figure G.4).

Freezing level height does not evidence any clear difference between GFS or FNL data, as the ensemble mean always underrate the height before the rainfall peak, in ~ 500 m (Figure G.5). This underestimation is smaller as the lead time decreases, depicting 72 hours of lead time as the best option between these given times.

For a better understanding of rainfall prediction, in hydrological terms, Table G.7 shows the rainfall event amount, length and the 5 most rainy hours (NRH). Is clear now that the GFS input data scores better for NRH(5), an important hydrological model input, even when the mean of both input data are very similar. The rainfall total amount is overestimated for all the simulations. As seen in Table G.7, FNL_{96} has rainfall properties overestimated, possibly caused by the reanalysis process applied to the data. GFS_{120} simulation has the best performance, for the three rainfall properties, but there is no clear trend associated to lead time. In general, similar results were obtained with both datasets, except with FNL dataset related to total rainfall length, leading GFS data to provide more feasible results. In accordance to the aforementioned values, GFS dataset is used in further simulations, since the improvement of FNL input data has not show a clear improvement for the rainfall properties.

TABLE G.6. Initial and boundary condition data (GFS/FNL) test statistics for 3 different lead times

120 h lead time	Temperature		Wind speed		Wind direction		Rainfall	
	GFS	**FNL**	**GFS**	**FNL**	**GFS**	**FNL**	**GFS**	**FNL**
MAE	2.55	2.36	2.17	1.91	77.90	75.92	1.49	1.66
NSE	−0.12	0.03	−21.5	−15.7	0.27	0.31	−2.1	−2.4
IoA	0.49	0.52	−0.61	−0.55	0.61	0.62	0.21	0.12
96 h lead time	Temperature		Wind speed		Wind direction		Rainfall	
	GFS	**FNL**	**GFS**	**FNL**	**GFS**	**FNL**	**GFS**	**FNL**
MAE	2.15	2.07	2.10	2.03	77.02	72.27	1.65	1.81
NSE	0.22	0.29	−17.7	−16.1	0.24	0.32	−2.4	−2.8
IoA	0.55	0.57	−0.58	−0.57	0.62	0.64	0.21	0.14
72 h lead time	Temperature		Wind speed		Wind direction		Rainfall	
	GFS	**FNL**	**GFS**	**FNL**	**GFS**	**FNL**	**GFS**	**FNL**
MAE	2.08	2.02	2.60	2.60	73.32	76.88	1.80	1.98
NSE	0.16	0.28	−37.8	−37.2	0.34	0.30	−1.9	−2.4
IoA	0.58	0.60	−0.69	−0.69	0.64	0.62	0.23	0.15

TABLE G.7. Rainfall properties for 3 different lead times

	Total amount [mm]		Total length [hours]		NRH(5) [mm]	
	110		80		36	
Lead time	**GFS**	**FNL**	**GFS**	**FNL**	**GFS**	**FNL**
120 h	193	243	76	38	37	41
96 h	186	173	78	25	51	50
72 h	213	207	70	94	46	49
Simulations mean	197	208	75	52	45	47

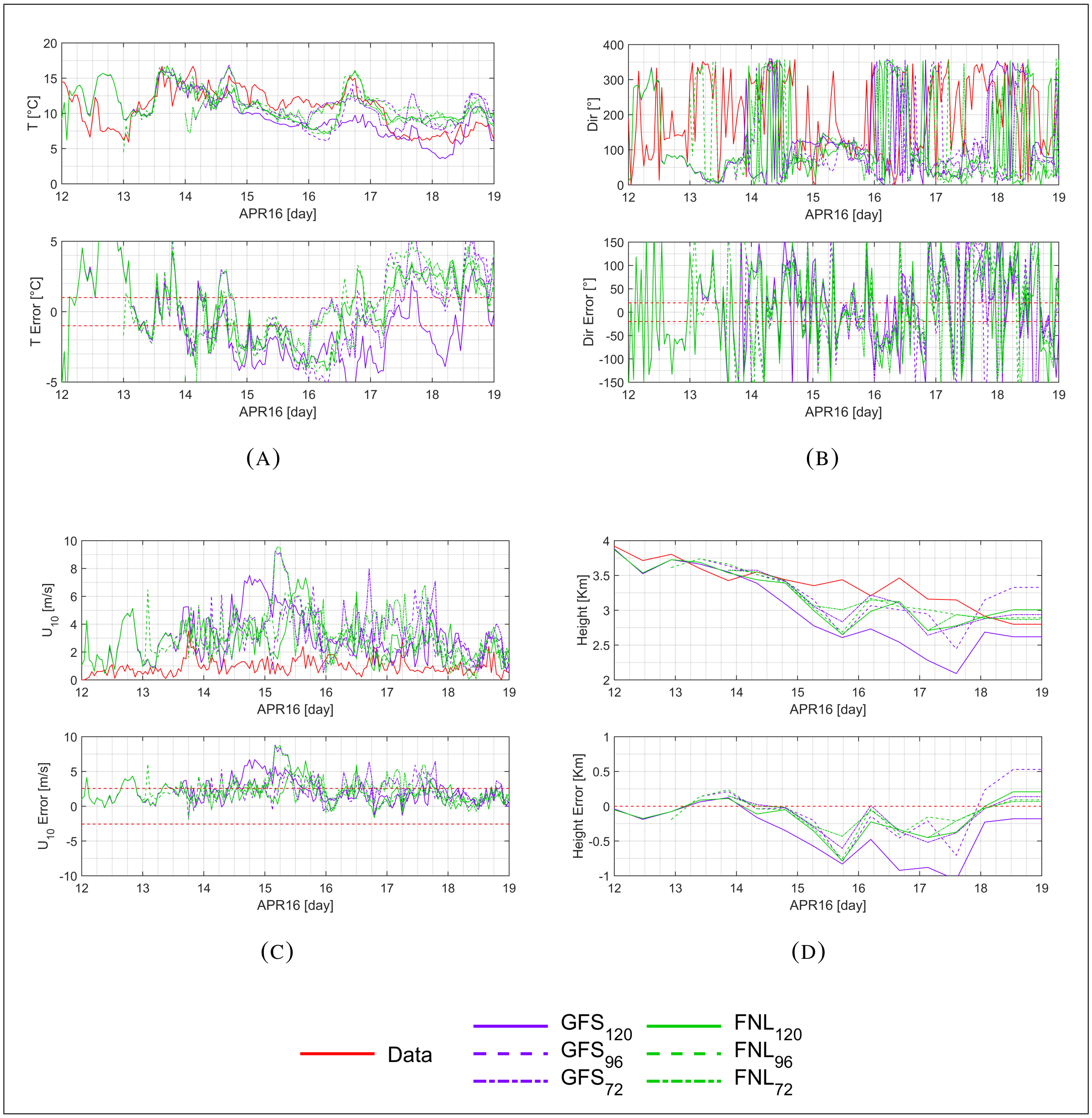

FIGURE G.4. Time series and error for GFS/FNL testing: (A) temperature, (B) wind direction, (C) wind speed and (D) freezing level height, for three lead times. In each subfigure the upper plot correspond to time series against observed data, and the lower plot is error in every simulation step: red dashed line in (A)-(C) is the tolerance criterion (Table 3.2) and ideal error (D).

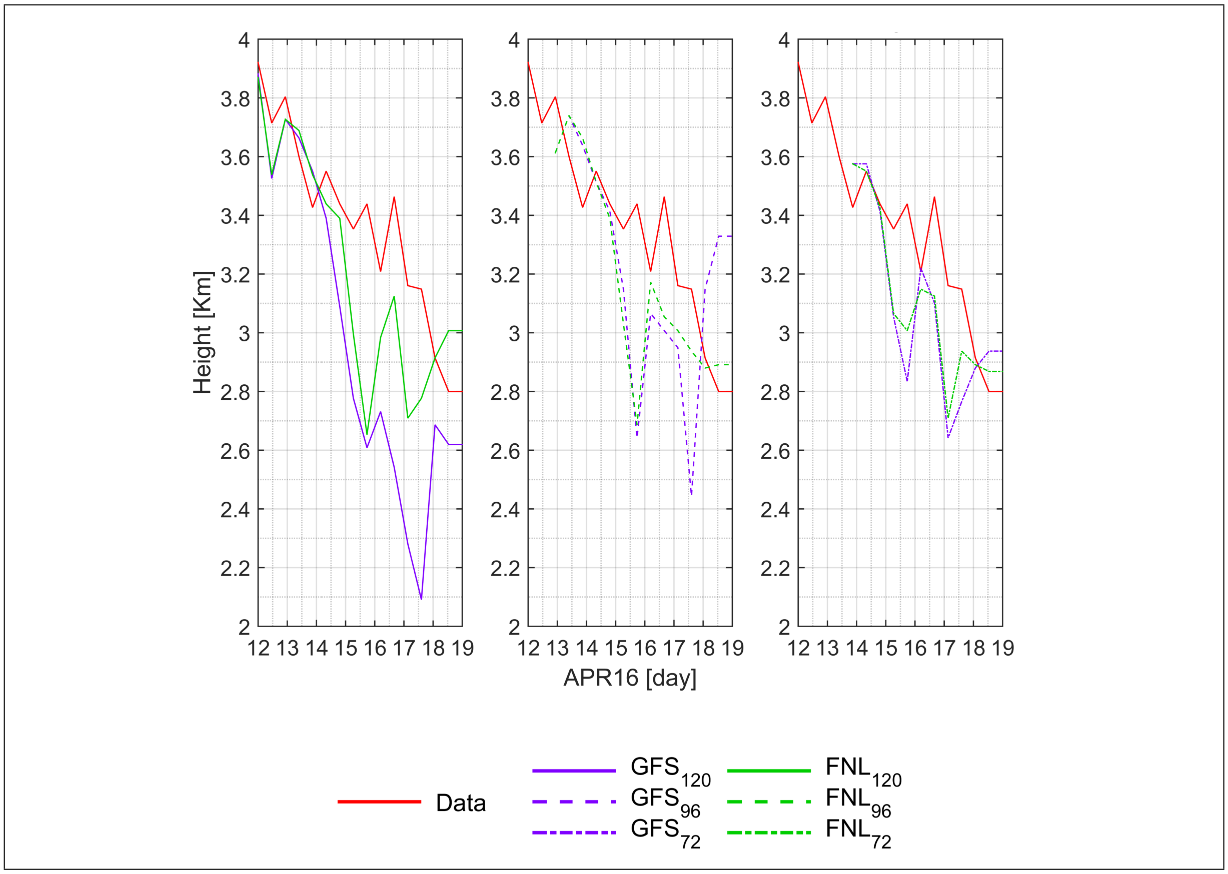

FIGURE G.5. Freezing level height for GFS/FNL and lead time testing: 120 hours (left), 96 hours (center) and 72 hours (right).

APPENDIX H. WRF RAINFALL SIMULATION

H.1. Hourly rainfall

Hourly rainfall is shown for OCT15 (Figure H.1), APR16 (Figure H.2) and MAY17 (Figure H.3) rainfall events.

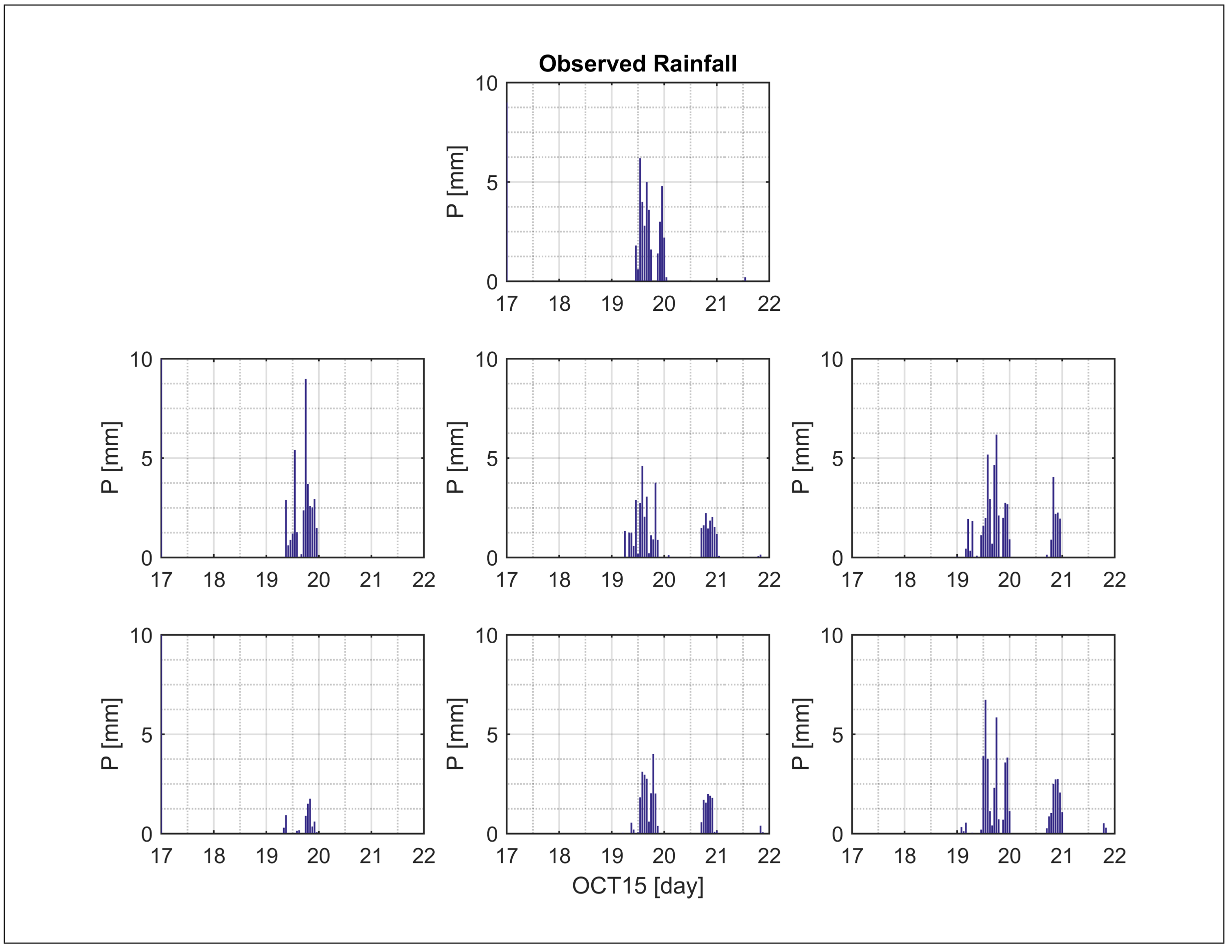

FIGURE H.1. OCT15 rainfall event, from 17^{th} to 22^{th} October 2015. Simulations made with 120 (left), 96 (center) and 72 hours (right) lead time; and MP LIN (central row) and WSM6 (lower row) options.

H.2. Rainfall properties

Rainfall properties, such as total amount (Figure H.4), duration (Figure H.5), and NRH(5) (Figure H.6), were calculated for OCT15 , APR16 and MAY17 rainfall events.

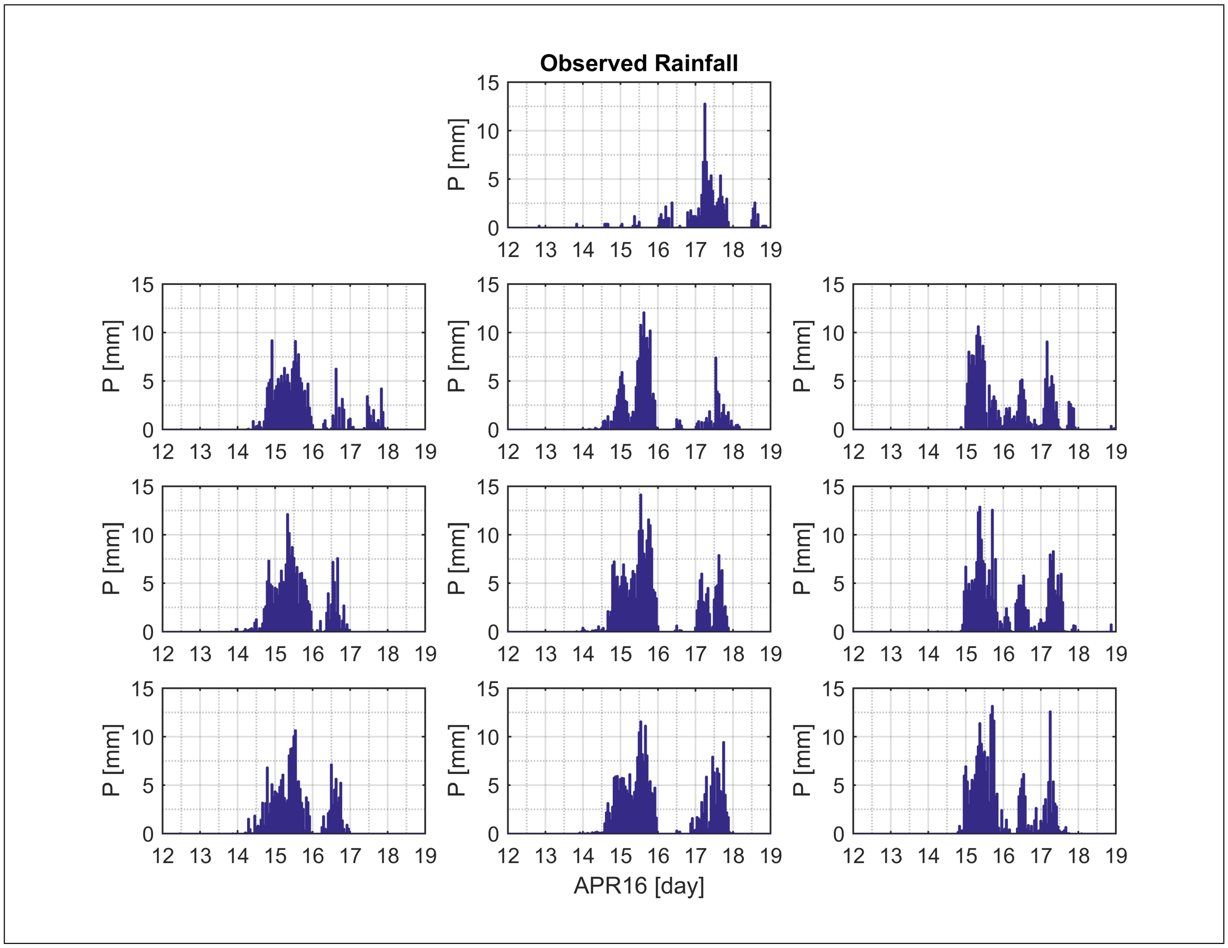

FIGURE H.2. APR16 rainfall event, from 14^{th} to 19^{th} April 2016. Simulations made with 120 (left), 96 (center) and 72 hours (right) lead time; and MP WSM3 (upper row), LIN (central row), WSM6 (lower row) options.

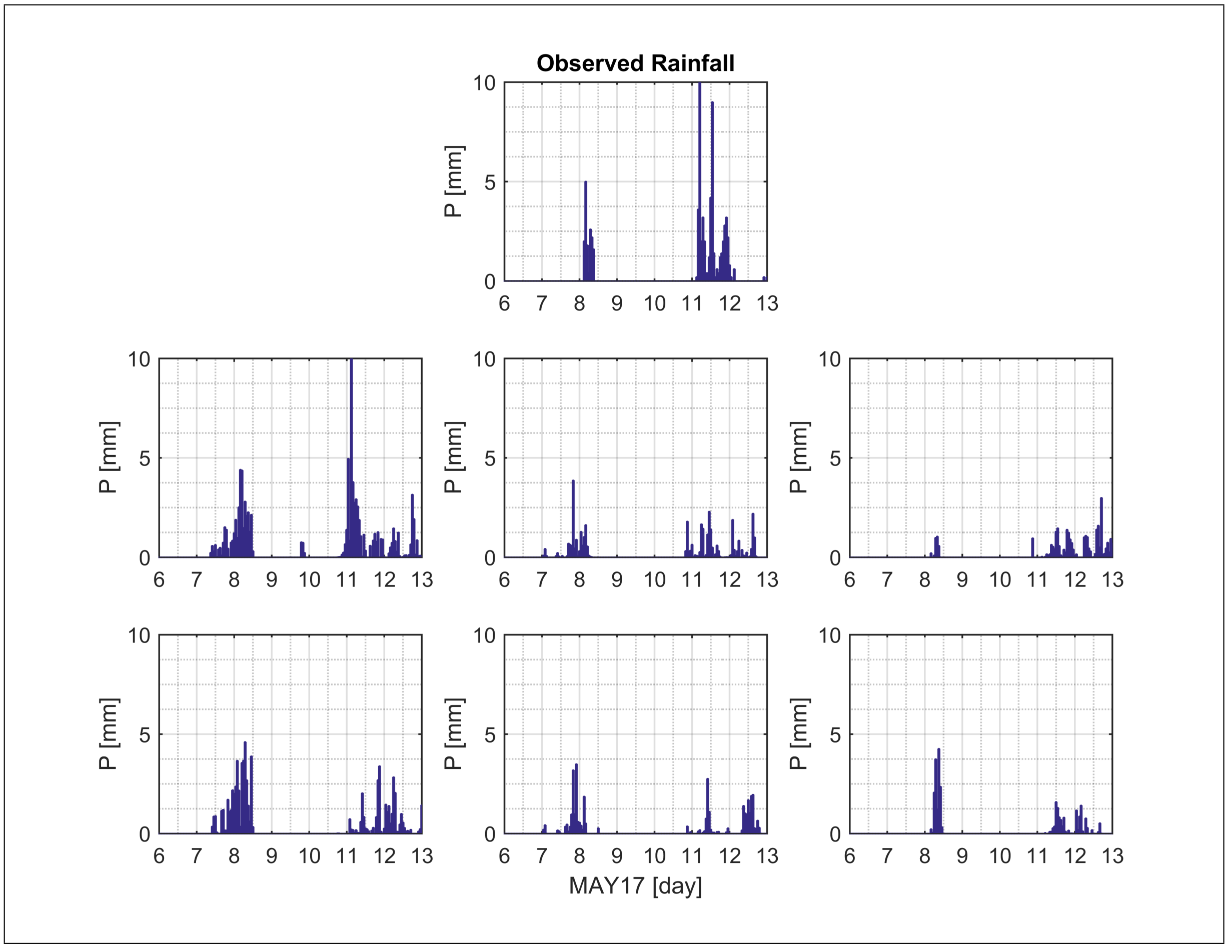

FIGURE H.3. MAY17 rainfall event, from 6^{th} to 13^{th} May 2017. Simulations made with 120 (left), 96 (center) and 72 hours (right) lead time; and MP LIN (central row) and WSM6 (lower row) options.

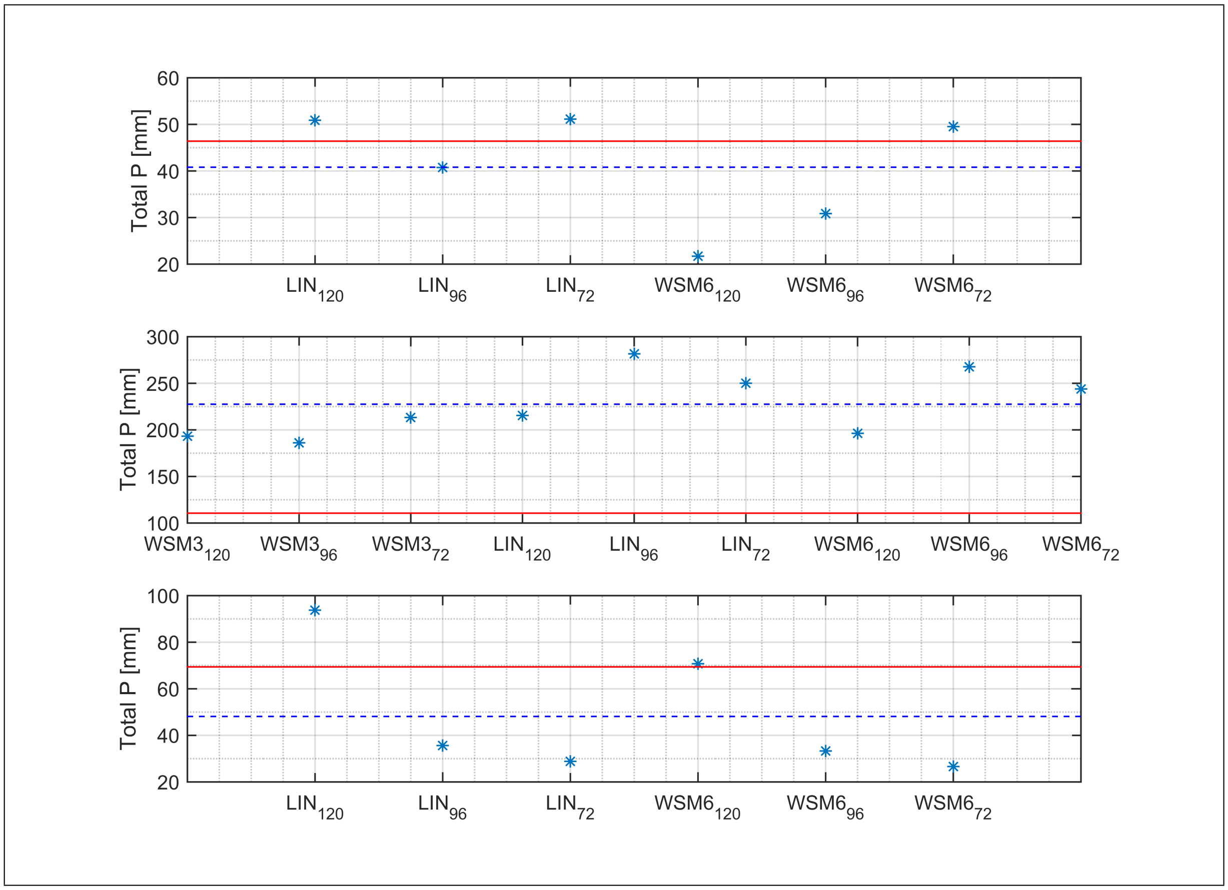

FIGURE H.4. Rainfall events magnitude, for OCT15 (upper plot), APR16 (central plot) and MAY17 (lower plot), with different MP options and lead times.Red line is observed data and blue dashed line is ensemble mean.

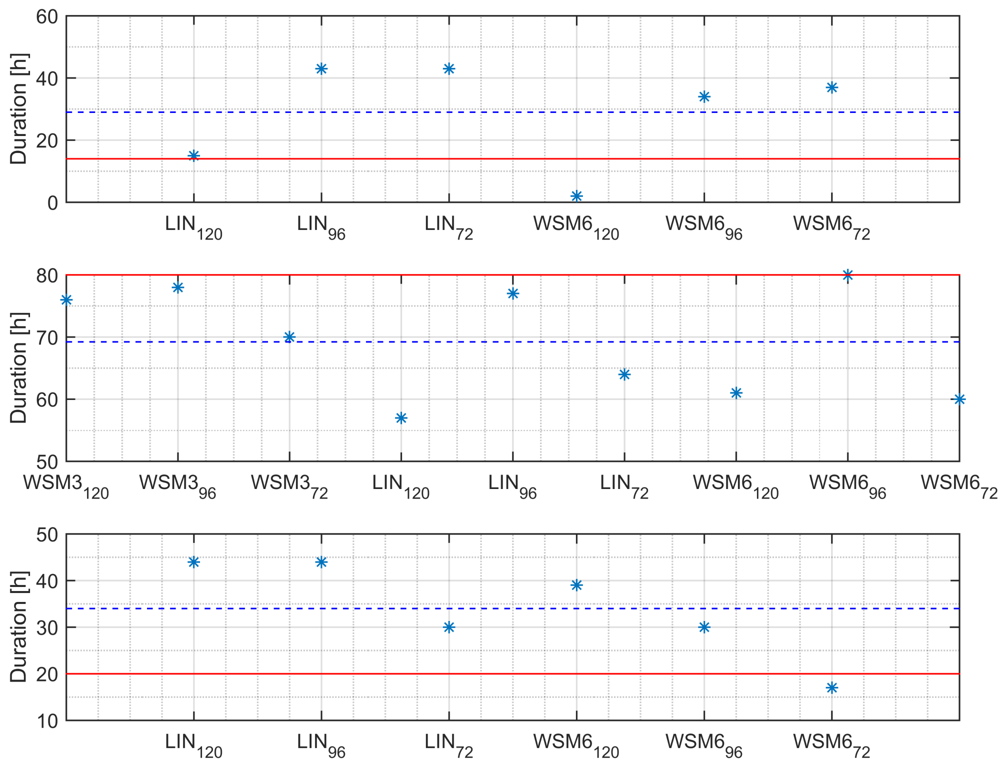

FIGURE H.5. Rainfall events duration, for OCT15 (upper plot), APR16 (central plot) and MAY17 (lower plot), with different MP options and lead times. Red line is observed data and blue dashed line is ensemble mean.

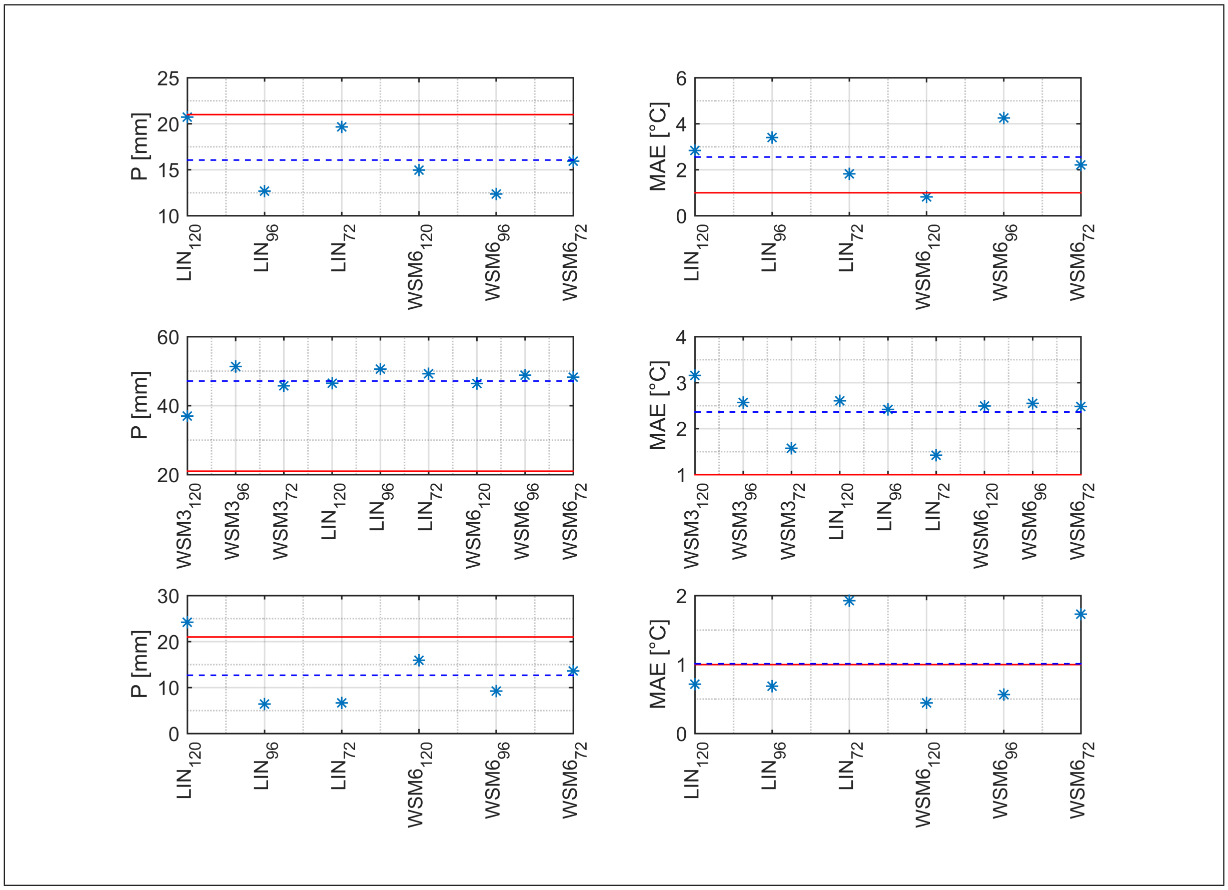

FIGURE H.6. NRH(5) (left) and MAE $T_{NRH(5)}$ (right), for OCT15 (upper plot), APR16 (central plot) and MAY17 (lower plot), with different MP options and lead times. In the left column, red line is observed data and blue dashed line is ensemble mean. In the right one, red line show DMC tolerance threshold.